

1 Stress fields of ancient seismicity recorded in the dynamic geometry of pseudotachylyte in the Outer  
2 Hebrides Fault Zone, UK

3

4 L.R. Campbell<sup>a,b\*</sup>, G.E. Lloyd<sup>a</sup>, R.J. Phillips<sup>a</sup>, R.C. Walcott<sup>c</sup>, R.E. Holdsworth<sup>d</sup>

5 <sup>a</sup> School of Earth and Environment, University of Leeds, LS2 9JT, UK

6 <sup>b</sup> Present address: School of Geography, Earth and Environmental Sciences, Plymouth University,  
7 PL4 8AA, UK.

8 <sup>c</sup> National Museums Scotland, Chambers Street. Edinburgh, EH1 1JF, UK

9 <sup>d</sup> Department of Earth Sciences, Durham University, DH1 3LE, UK

10

11 LC ORCID: 0000-0003-0337-0712

12 \* Corresponding author ([lucy.campbell@plymouth.ac.uk](mailto:lucy.campbell@plymouth.ac.uk))

13 Abbreviated title: Stress fields recorded in pseudotachylyte

14

15 Abstract

16 Heterogeneous sequences of exhumed fault rocks preserve a record of long-term evolution of fault  
17 strength and deformation behaviour during prolonged tectonic activity. Along the Outer Hebrides  
18 Fault Zone (OHFZ), UK, numerous pseudotachylytes record palaeoseismic slip events within  
19 sequences of mylonites, cataclasites and phyllonites.

20 To date, the kinematics and controls on seismicity within the long active history of the OHFZ have  
21 been poorly constrained. Additional uncertainties over the relative location of a meteorite impact  
22 and possible pre-OHFZ brittle faulting also complicates interpretation of the diffuse seismic record.  
23 This study presents kinematic analyses of seismicity in the OHFZ, combining observations of offset  
24 markers, en-echelon injection veins, and injection vein geometry to reconstruct slip directions and  
25 stress fields. This new dataset indicates that a range of fault orientations, slip directions and slip  
26 senses hosted seismicity in the OHFZ. Such complexity requires several stress field orientations, in  
27 contrast to NW-SE Caledonian compression traditionally attributed to frictional melting along the  
28 OHFZ, indicating that seismicity had a long-term presence across the fault zone. Persistence of  
29 strong frictional failure alongside the simultaneous development of weak fault rocks and phyllonitic  
30 shear zones in parts of the OHFZ has significant implications for understanding seismic hazard along  
31 mature continental faults.

32 Supplementary material is available at:

33

34 Pseudotachylytes are solidified frictional melts generated by seismic rupture along sliding surfaces  
35 (Philpotts, 1964; Sibson, 1975; Maddock, 1983; Cowan, 1999, Rowe et al. 2018). In non fault-slip  
36 related contexts they may also be generated by impact cratering (e.g. Spray, 1998) or along the  
37 frictionally sliding base of large landslides (e.g. Legros et al., 2000). Fault-generated  
38 pseudotachylytes, however, are particularly useful in that they record a snapshot of coseismic  
39 behaviour along a fault, and are widely accepted to be fault rocks that unequivocally demarcate  
40 seismicity (Rowe and Griffith, 2015). In the structural record of long-lived and reactivated fault  
41 zones, pseudotachylytes provide useful markers for the location, kinematics and timing of seismic  
42 activity. Pseudotachylytes from the Outer Hebrides Fault Zone (OHFZ), Scotland (Fig. 1), were first  
43 used for seismic analysis by Sibson (1975, 1977a, 1980), and the fault zone has since become a  
44 classic area for this fault rock type (Macaudière and Brown, 1982; Maddock, 1983; White, 1996;  
45 MacInnes et al., 2000; Osinski et al., 2001). The OHFZ is a crustal-scale fault (Smythe et al., 1982)  
46 traditionally thought to have accommodated significant Caledonian convergence within the  
47 basement of the Laurentian foreland to the orogenic belt (Streule et al., 2010). However, the fault  
48 zone has in fact accommodated a larger range of movement over its active history in addition to  
49 thrusting, including late strike-slip movement and subsequent extension as the Caledonian orogeny  
50 progressed (Butler et al., 1995; Imber et al., 2001; Szulc et al., 2008). Additionally, the earliest  
51 movement on the OHFZ may have initiated as ductile thrusting at a much earlier date, at around  
52 1100 Ma (see Imber et al., 2002 for discussion).

53 It is not always clear whether the seismicity indicated by OHFZ pseudotachylytes was associated with  
54 Caledonian thrusting, as initially envisaged by Sibson (1975). Fault orientations (Fig. 1) and slip  
55 directions on pseudotachylyte-bearing faults in the OHFZ are not always consistent with top-to-the  
56 NW reverse movements typically attributed to Caledonian compression (White and Glasser, 1987;  
57 MacInnes et al., 2000; Osinski et al., 2001). Further observations are needed to fully investigate  
58 whether seismicity across the OHFZ, recorded by pseudotachylytes with observed fault lengths  
59 typically < 10 m, occurred predominantly within one kinematic phase (such as Caledonian thrusting)

60 with additional accommodation of movement on smaller secondary normal and/or strike-slip faults,  
61 or whether multiple regional-scale kinematic regimes and associated stress fields triggered  
62 seismicity throughout the active history of the OHFZ.

63 Major fault zones are typically considered to progressively decrease in strength after repeated  
64 periods of slip and the associated onset of weakening mechanisms such as grain size reduction and  
65 mineral phase changes (Imber et al., 1997; Collettini et al., 2009; Holdsworth et al., 2011; Behr and  
66 Platt, 2014). Constraining the timing of active seismicity, controlled by this evolution of fault  
67 strength, is an important concept in understanding where earthquakes may continue to nucleate  
68 along mature faults that otherwise appear to be creeping aseismically and hence are assumed to be  
69 weak. In the case where seismicity occurs along well-established fault zones, different spatial  
70 distributions of seismic and aseismic behaviour have been proposed, with earthquake nucleation  
71 restricted to either deeper locked sections beneath the aseismic portion (e.g. Wallis et al., 2013) or  
72 along fault segments that have escaped spatially heterogeneous fault weakening processes such as  
73 fluid influx (e.g. MacInnes et al., 2000).

74 Despite the abundance of pseudotachylyte-bearing faults in the OHFZ (Sibson, 1975), the  
75 magnitudes of displacement and senses of slip are often difficult to determine due to the rarity of  
76 identifiable offset markers. As a result, the kinematic context and timing of seismicity on the OHFZ  
77 has remained rather poorly constrained. Here we supplement field offset marker observations with  
78 data derived from a range of kinematic indicators inherent to the geometry of pseudotachylyte fault  
79 networks, including fault orientation and injection veins related to dynamic tensile fracturing, in  
80 order to assess the kinematic regime(s) recorded by the OHFZ pseudotachylytes. In doing so, we aim  
81 to better constrain the seismic environment of this 'classic' area and to explore the history of  
82 seismicity in relation to the development and maturation of a crustal scale fault.

### 83 **Geological Background**

84 The OHFZ is exposed for almost 200 km onshore along the eastern seaboard of the Outer Hebrides  
85 (or Western Isles, Na h-Eileanan Siar), NW Scotland, UK (Fig. 1). It typically dips 20-25° towards ESE  
86 on regional scale seismic imaging (Smythe et al., 1982) and cuts the Archean-Paleoproterozoic  
87 Lewisian complex (Fettes et al., 1981). The Lewisian in the Outer Hebrides predominantly consists of  
88 granulite and amphibolite facies banded felsic and pyroxene gneisses, together with subordinate  
89 units of meta-basic dykes, meta-anorthosite, meta-gabbro, and localised metasediments (Fettes et  
90 al., 1981).

91 Initiation of the OHFZ likely took place at ~1100 Ma, potentially related to Grenvillian tectonics  
92 (Butler et al., 1995; Imber et al., 2002). This is the maximum possible age for OHFZ movement, as it  
93 cuts late tectono-thermal structures dated to this time (Cliff and Rex, 1989) and consistently  
94 overprints Laxfordian age (~1700 Ma) pegmatites (Imber et al. 2002). The kinematic history of the  
95 OHFZ has been much debated since early work interpreted it to be dominantly thrust related  
96 (Coward, 1969; Francis and Sibson, 1973; Sibson, 1975). Many workers (Sibson, 1975; Butler et al.,  
97 1995; MacInnes et al., 2000; Osinski et al., 2001; Imber et al., 2002) agree that initial movement  
98 consisted of ductile top-to-NW thrusting, followed by later, shallower top-to-NW brittle thrusting  
99 during the Caledonian Orogeny. Later post-thrusting movement included spatially heterogeneous  
100 components of sinistral strike-slip (Butler et al., 1995; Imber et al., 2002) or a mix of sinistral and  
101 dextral strike-slip (MacInnes et al., 2000), followed by extension (White and Glasser, 1987; Butler et  
102 al., 1995; MacInnes et al., 2000; Imber et al., 2001; Osinski et al., 2001). The contribution of some  
103 extensional movement during the main brittle thrusting phase is disputed (White and Glasser, 1987;  
104 Imber et al., 2001; Osinski et al., 2001), as is the pervasiveness of late sinistral strike slip, leading to  
105 suggestions of a heterogeneous kinematic history along different fault segments (Butler et al., 1995;  
106 MacInnes et al., 2000; Osinski et al., 2001).

107 Within this evolving kinematic history, the type and sequence of fault rocks observed also varies  
108 between different segments of the OHFZ (Table 1). Amphibolite-facies mylonites relating to early

109 ductile initiation extend to thicknesses of 600 m in the north of the onshore OHFZ (Fig. 1), across the  
110 islands of Lewis and Sgalpaigh (Scalpay) (Butler et al., 1995). Further to the south, however,  
111 mylonites are only seen highly localised onto individual fault planes (Osinski et al., 2001). Brittle fault  
112 planes postdating these early ductile shear zones are widespread along the western extent of the  
113 main fault zone (shown as the fault trace in Fig. 1), incorporating pseudotachylyte and cataclasite  
114 (Sibson 1977; Butler et al., 1995; Imber et al., 1997). Fluid influx triggering greenschist-facies  
115 alteration and phyllonitisation occurred along the east of the fault zone, and it is these phyllonites  
116 and other low-temperature mylonites that record much of the late- to post-Caledonian strike slip  
117 and extensional phases (Butler et al., 1995; Osinski et al., 2001; Szulc et al., 2008). This fluid-rock  
118 interaction was not ubiquitous across the fault zone, resulting in lenses of phyllonite within  
119 retrogressed gneisses and locally preserving unaltered segments along the fault zone that appear to  
120 have escaped fluid influx altogether (Sibson, 1980; MacInnes et al., 2000).  $^{40}\text{Ar}/^{39}\text{Ar}$  dating of OHFZ  
121 pseudotachylytes has generated Caledonian ages of  $430 \pm 6$  Ma (Kelley et al., 1994), whilst others  
122 have yielded ages of 1900 Ma,  $\sim 1200$  Ma and 700 Ma (Sherlock et al., 2009). Alternative causes for  
123 some or all of the Outer Hebrides pseudotachylytes have therefore been suggested as: a) early  
124 pseudotachylyte generation coeval with ductile thrusting on the OHFZ, observed so far only in the  
125 northern extent of the OHFZ (Sibson 1980; White 1996); b) distal seismicity as a response to  
126 tectonic regimes such as the Knoydartian orogeny - which may have also triggered pre-Caledonian  
127 initiation of the mainland Moine Thrust (Sherlock et al. 2009; Krabbendam et al. 2017); or c) impact-  
128 generated pseudotachylyte relating to an impact recorded by the Stac Fada member of the  
129 Mesoproterozoic Stoer Group on the Scottish mainland (Amor et al. 2008; Sherlock et al. 2009;  
130 Reddy et al. 2015, Amor et al., 2019). However, many of the pseudotachylytes are spatially related  
131 to the OHFZ (Fig. 1) and no unambiguous evidence for impact-related processes has yet been  
132 observed from the Outer Hebrides.

133 Pseudotachylytes occur in the OHFZ with a range of morphologies, including linear fault and  
134 injection veins, networks of veins, pseudotachylyte-matrix breccias and linkages between paired

135 faults (Fig. 2). Such structures record the sometimes complex geometry of the individual ruptures  
136 that generated the pseudotachylytes (Rowe et al. 2018). Pseudotachylyte-bearing faults are  
137 scattered quite widely across the Outer Hebrides, including in regions where other major fault  
138 structures are not apparent – for example, the west coasts of Barra and South Uist (Fig. 1). The melt-  
139 origin of these pseudotachylytes is recognised from features such as quench-crystallisation  
140 morphologies (e.g. spherulites, microlites and dendritic crystals), concave embayments into survivor  
141 clasts within the pseudotachylyte, and from the preferential breakdown of low-melting point  
142 minerals such as biotite and amphibole (Fig. 2). The fine-grained crystalline matrix of these OHFZ  
143 pseudotachylytes is typically composed of oligoclase plagioclase, hornblende and some biotite,  
144 broadly reflecting the host rocks present along the generation plane (O’Callaghan & Osinski, 2019),  
145 whilst unmelted clasts of the host rock are dominated by quartz and plagioclase. Alteration  
146 assemblages within the pseudotachylyte veins, where seen, are commonly chlorite and epidote,  
147 more rarely with actinolite and albite.

148 Pseudotachylyte generation planes, including linear fault veins (Fig. 2a) as well as fault breccias with  
149 a melt-derived matrix (Fig. 2b), show a variety of orientations (Fig. 1). A cluster of faults dip  
150 moderately NE through east to SE, with the modal dip direction oriented between 070-080°. There is  
151 no systematic variation in fault orientation seen with respect to the spatial location of the faults  
152 observed along strike on the OHFZ as the main fault trace curves northwards from NNE-SSW to NW-  
153 SEE (Fig. 1). Very locally, some systematic changes in orientation do exist, for example on Grimsay  
154 where a series of small backthrusts form a cluster dipping west or NW (Fig. 1, ‘Northern Uists’  
155 stereonet). In southeastern South Uist the faults tend to be dipping more towards the NE and NNE  
156 compared to Barra to the south, which has a spread of dip directions from SE round to NE. The main  
157 trace of the OHFZ is also more NNE-SSW in southeastern South Uist compared to NE-SW in Barra,  
158 but this correlation does not seem to be maintained across other regions of the OHFZ (Fig. 1).

## 159 **Methods**

160 Fieldwork for this study investigated several sites along and around the main segments of the OHFZ  
161 (Fig. 1). Field observations focussed on recording the geometry and orientation of pseudotachylyte-  
162 bearing faults and associated features, with the aim of interpreting the sense of displacement. Fault-  
163 derived pseudotachylytes do not typically record slickenlines or other direct evidence of slip  
164 direction; although 'brushlines' formed by the coseismic drag of fault wall asperities across  
165 pseudotachylyte melt have been observed at the host rock – pseudotachylyte interface (Ferré et al.  
166 2016), this surface is rarely exposed due to the tendency for pseudotachylytes to weld to the fault  
167 plane (Mitchell et al. 2016). Instead, three different approaches were utilised: (1) recording offsets  
168 indicated by displaced marker structures across pseudotachylyte-bearing faults; (2) recording  
169 orientations of systematic injection veins considered to have formed due to dynamic off-fault tensile  
170 cracking under the coseismic rupture-tip stress field; and (3) recording the orientations of en-  
171 echelon arrays of injection veins.

#### 172 *Field and microstructural markers of displacement direction*

173 Direct field observations of planar markers offset across a fault, for example mineral banding or  
174 veins (Fig. 3a-d), were used to record the apparent slip sense of each fault. In addition, fault dip  
175 direction was recorded in order to investigate any link between fault orientation and slip sense. For  
176 example, the pseudotachylyte-bearing fault in Fig. 3a is recorded with apparent extensional offset of  
177 an earlier pseudotachylyte vein across a SE-dipping fault. Similarly, microstructural indicators of slip  
178 sense visible in thin sections of pseudotachylyte fault veins included small-scale offset markers,  
179 aligned clasts in the pseudotachylyte vein, and asymmetrical shear structures in the margins judged  
180 to be contemporaneous with melting (Figs. 3e,f). These were combined with field observations  
181 where the fault vein orientation was known. Unfortunately, it was not possible to reconstruct full  
182 slip vectors from this dataset, due to the lack of multiple displaced markers or striation-style  
183 transport direction indicators (c.f. Yamada & Sakaguchi, 1995, Xu et al., 2009). The observed offsets  
184 (apparent displacements) for this dataset range from 0.010 – 0.410 m, consistent with a range of



185 0.003 – 1.670 m reported for OHFZ pseudotachylite faults in previous studies (Sibson, 1975, Hirose  
186 & Shimamoto, 2005, Nielsen et al., 2010).

187 *Application of dynamic off-fault tensile crack model for determination of slip direction*

188 During coseismic rupture and frictional melting along a fault plane, injection of melt away from the  
189 fault to form secondary veins into the surrounding host rock may occur (Figs 4a-d). These injection  
190 veins may exploit pre-existing fractures if they are present, but can also form via dynamic coseismic  
191 fracturing (Di Toro et al., 2005; Griffith et al., 2009; Ngo et al., 2012). Known as dynamic off-fault  
192 tensile cracks (e.g. Ngo et al., 2012), they initiate during rupture of the fault within the dynamic  
193 tensile stress field around the rupture-tip, and hence systematically fracture a single fault wall as the  
194 rupture-tip passes (Griffith et al., 2009; Ngo et al., 2012). The clearest distinction in natural faults of  
195 these dynamic cracks from other fracture sets is seen when a series of parallel cracks develops on  
196 one side of the fault (Fig. 4e). Such features have been observed in the form of tensile injection veins  
197 along pseudotachylite faults (Di Toro et al., 2005; Ngo et al., 2012). The magnitude of the angle  
198 between a tensile crack and the fault is controlled by many factors, including slip velocity, fault  
199 frictional strength, velocity weakening behaviour, confining pressure and Poisson's ratio (Ngo et al.,  
200 2012, Alneasan et al., 2020), but in all cases, the sense of slip is towards the acute intersection  
201 between the crack and the fault (Fig. 4f, Di Toro et al., 2005; Griffith et al., 2009; Ngo et al., 2012).  
202 The slip vector is oriented perpendicular to the line of intersection between the tensile injection vein  
203 with the fault plane (Fig. 4f). Identifying the orientation of this intersection therefore allows the  
204 seismic slip direction to be determined.

205 Pseudotachylite fault planes in the OHFZ were included for analysis of slip directions from off-fault  
206 tensile cracks if they displayed multiple sub-parallel injection veins restricted to a single side of the  
207 fault plane (Fig. 4a-d). Faults with single injections were also included if there were no injections on  
208 the opposing wall and if adjacent parallel faults with similarly oriented injection veins were observed  
209 within 0.5 m perpendicular to the fault. Orientations of injection veins and fault veins were

210 recorded, and the acute angle between injection veins and the fault was identified to determine the  
211 sense of slip (Fig. 4f). Because the best exposed examples of these features are often in flat vertical  
212 (Fig. 4a-b) or horizontal (Fig. 4c-d) faces, measurement of the injection veins can sometimes carry  
213 greater uncertainty than the  $\sim\pm 1^\circ$  typical of field measurements, depending on the smoothness of  
214 the exposure surface, the occurrence of fractures cutting across and exposing different faces, and  
215 the extent of differential weathering of the pseudotachylyte relative to the host rock. The  
216 uncertainty of measurement was considered in the context of sets of injection veins at any one  
217 locality; either the orientation of the most reliable injection vein, or alternatively an average of  
218 multiple injection veins where of equal certainty, was used to derive the trend of slip via the  
219 perpendicular to the intersection (Supplementary Table 2). Fault slip analysis to determine the  
220 probable stress field during slip was then undertaken using a combination of the derived slip trend  
221 and fault orientation data. During this process, fault plane solutions for each pseudotachylyte-  
222 bearing fault were calculated using a kinematic approach from the maximum axes of compression  
223 and extension (e.g. Marrett and Allmendinger, 1990).

224 Further dynamic fault slip inversion for palaeostress analysis was conducted to constrain the  
225 possible stress fields for seismicity recorded by these pseudotachylyte faults (e.g. Angelier 1994,  
226 Žalohar and Vrabec, 2007). Several methods for fault inversion exist, including various methods of  
227 separating heterogeneous fault slip observations generated by changing stress fields (e.g. Nemcok  
228 and Lisle, 1995; Shan and Fry, 2005; Sato and Yamaji, 2006). Here, the Gaussian method of Žalohar  
229 and Vrabec (2007), is chosen due to its relatively good ability to form stable stress tensor solutions  
230 with differing and/or small fault numbers in each stress tensor subset, or with error in the slip sense  
231 of the fault planes, and to distinguish between stress tensors with small angular differences ( $> 10^\circ$ ).  
232 Importantly, the method (automated in the freely available software “T-Tecto X5”,  
233 [http://www2.arnes.si/~jzaloh/t-tecto\\_homepage.html](http://www2.arnes.si/~jzaloh/t-tecto_homepage.html)) demands mechanical compatibility of the  
234 fault planes and their slip directions in order to contribute to a stress tensor solution – each fault  
235 must satisfy Amontons’ Law,  $\mu < \tau/\sigma_n$ , where  $\mu$  is the friction coefficient,  $\tau$  the shear stress and  $\sigma_n$

236 the normal stress on the fault plane. The inversion returns the best-fit reduced stress tensor - the  
237 orientations of the principal stresses ( $\sigma_1 \geq \sigma_2 \geq \sigma_3$ ) and the stress ratio defining the relative stress  
238 magnitudes ( $\phi = [\sigma_2 - \sigma_3] / [\sigma_1 - \sigma_3]$ ).

239 The method handles heterogeneous fault slip populations (i.e. faults and their slip directions that  
240 relate to several varying stress fields) by applying a best-fit stress tensor to a population of  
241 compatible faults. The workflow is described in full in Žalohar and Vrabec (2007), but here we  
242 summarise the approach. Firstly, the analysis takes the bulk input fault slip data and applies an  
243 object function that assesses the mechanical compatibility for all faults over a range of possible  
244 stress tensor orientations; the maxima of this object function distribution is used to locate the stress  
245 tensor for this first stage. Faults that have angular misfits between their ideal slip direction (i.e. the  
246 direction of maximum shear stress as per the Wallace-Bott hypothesis; Bott, 1959, Wallace, 1951)  
247 less than the user-defined misfit threshold ( $\alpha$ ) are considered compatible with this stress tensor. The  
248 process restarts using only the faults determined to be incompatible with the first stress tensor. The  
249 next best-fit stress tensor is constrained and again the angular misfit threshold  $\alpha$  can be set to  
250 determine which faults can be included as compatible with this stress tensor. At this stage, faults  
251 that were associated with the first stress tensor can also be included if they meet the angular misfit  
252 threshold for the second stress tensor, which reduces the chance of ambiguous faults being wrongly  
253 removed from the analysis at an early stage. The second stress tensor can be reanalysed including  
254 such faults. The process is repeated further until all faults are accounted for. Several parameters can  
255 be set to refine the angular dispersion and the mechanical compatibility – our choice of values for  
256 these are detailed in the Supporting Information.

257 The available observations of fault slip directions are limited in number ( $n=35$ ). Consequentially,  
258 these results are considered in conjunction with other field observations presented in this study in  
259 order to minimise the possibility of artefacts in the stress tensors produced from the fault inversion  
260 (Orife and Lisle, 2006).

261 Application of en-echelon models to pseudotachylyte injection veins

262 A common pseudotachylyte vein morphology across the OHFZ and elsewhere (e.g. Sibson,  
263 1975; Hoek, 1991, Clarke & Norman, 1993, Garde & Klausen, 2016) is an en-echelon  
264 segmented array (Fig. 5). As these en-echelon veins lack displacement along them, they are  
265 likely to be injection veins (Garde & Klausen, 2016). This lack of displacement along with the  
266 tensile mode of fracturing needs to be identified, because similar geometries are also seen  
267 in stepped pseudotachylyte-bearing fault segments (e.g. Campbell et al., 2019). Where a  
268 three-dimensional example can be seen (Fig. 5e), the en-echelon segments are observed to  
269 branch out from a single vein. Three-dimensional exposures of these veins have not been  
270 found in-situ, but an array in an uncommon vertical exposure face (Fig. 5d) shows  
271 segmentation occurring at the tip of an injection vein in the direction of injection  
272 propagation away from a fault vein. In many cases (Figs. 5a-c) segmentation of steeply  
273 dipping veins is observed on near-horizontal surfaces and the fault plane is not seen. The  
274 array of en-echelon injection segments is sometimes diffuse, which may represent multiple  
275 veins (Fig. 5b) but, where a more linear arrangement exists, the long axis of individual veins  
276 may be either oblique (Fig. 5a) or parallel (Fig. 5c) to the overall array trend. Vein tips curve  
277 in towards an approaching or overlapping adjacent vein segment (Figs. 5c,d) but there is no  
278 obvious macroscopic deformation of the adjacent rock between veins. The direction of step  
279 between adjacent segments is not necessarily constant within any array.

280 The characteristics of these segmented pseudotachylyte arrays are more typical of en-  
281 echelon fracture models (e.g. Pollard et al., 1982) than of sigmoidal vein arrays formed in  
282 shear zones (e.g. Beach, 1975; Lisle, 2013). During propagation of a tensile crack (Fig. 6a),  
283 en-echelon segmentation can be induced by the presence of a resolved shear stress on the

284 walls of the crack (Fig. 6b). For example, a change in the stress field encountered during  
285 continued crack propagation can result in a growing fracture, perhaps initially aligned to a  
286 local or transient principal stress, progressively segmenting and rotating its propagation  
287 trajectory in order to alignment with a remote or background principal stress field, ideally  
288 ending up perpendicular to the minimum compressive stress (Pollard et al., 1982).  
289 Depending on the point of exposure of the observed en-echelon array relative to the  
290 position along the entire crack, the en-echelon segments may not necessarily be visible at  
291 their point of maximum realignment towards any such stress field (Fig. 6c, Nicholson and  
292 Pollard, 1985) and the maximum realignment may not necessarily be perfectly  
293 perpendicular to the bulk extension direction (e.g. McCoss, 1986). The curvature seen at the  
294 en-echelon segment tips is related to the interaction of adjacent or overlapping dilatant  
295 segments (Pollard et al., 1982; Olson and Pollard, 1991).

296 En-echelon fracture and dyke models (e.g. Pollard et al., 1982; Nicholson and Pollard, 1985;  
297 Olson and Pollard, 1991) are applied here to pseudotachylyte injection veins (Fig. 6c). We  
298 test whether analysis of principal stress orientations similar to those performed on en-  
299 echelon fractures, dykes and veins (e.g. Pollard et al., 1982; Rickard and Rixon, 1983) can be  
300 made on pseudotachylyte geometries. In this context, the injection vein is initially a tensile  
301 fluid-filled crack at the point where it originates from the fault plane (Fig. 6c). This 'parent'  
302 injection vein is oriented perpendicular to the minimum compressive stress of the rupture-  
303 tip stress field, which is transiently parallel to the slip direction under the off-fault tensile  
304 crack model previously discussed (Ngo et al., 2012). As the rupture tip continues to  
305 propagate along the fault plane away from the initiation point of any given injection vein,  
306 and combined with the increasing distance of the vein tip from the fault plane as it  
307 propagates into the host rock, the influence of the transient rupture-tip stress field wanes.

308 Instead, a remote stress field becomes the dominant influence on the trajectory of the  
309 injection vein, encouraging segmentation at the propagating vein tip to facilitate progressive  
310 rotation of the injection vein trajectory (Figs. 6b-c). This far-field stress field may be the  
311 regional tectonic stress field, or some modification of it imposed by larger-scale active  
312 structures in the vicinity of the observed pseudotachylyte-fault. Where an en-echelon array  
313 of pseudotachylyte injection veins is observed in the field, the trend of the whole array  
314 corresponds to the initial trace of the parent injection vein when it branched from the fault  
315 plane. Conversely, the orientation of each individual segment indicates the magnitude of  
316 rotation of the injection vein propagation path (Fig. 6c). Here, the orientations of individual  
317 segments are compared with the orientation of the overall array, with results presented as  
318 trends normal to the strike of the array and of the segment. We use the assumption that  
319 these approximate the local and far-field minimum compressive stresses, respectively  
320 (Pollard et al., 1982).

## 321 **Results**

### 322 Field and microstructural observations of slip sense

323 Both normal and reverse apparent fault movements are indicated by field and microstructural  
324 indicators of slip sense observed along various pseudotachylyte faults, in addition to two sinistral  
325 strike slip faults (Fig. 7). Normal offsets are predominantly hosted on faults with dip directions  
326 between north and NW, or between south, SE and east (n = 15). In contrast, faults with a reverse  
327 component generally dip to the west, or towards the NE (n = 19). Too few faults with significant  
328 apparent strike-slip components were observed to draw any valid conclusions (Fig. 7).

### 329 Slip directions from secondary dynamic tensile veins

330 Slip trends calculated from dynamic tensile injection veins (Fig. 4) are indicated with fault slip  
331 solutions and palaeostress analysis stereonet in Fig. 8. Shallowly plunging slip vectors dominate,  
332 with clusters indicating NE-SW and NW-SE trends. Several faults within this dataset are NE-dipping  
333 (Fig. 8); such faults occur in many localities across the OHFZ and many show oblique reverse senses  
334 of movement with both dextral and sinistral components (Figs. 1, 8). SE- and NW- dipping faults are  
335 also common. In any given location, a variety of fault orientations occur, with differing slip  
336 kinematics. Palaeostress analysis suggests that at least three stress fields are needed to account for  
337 this variation. Firstly, where the maximum principal stress ( $\sigma_1$ ) is broadly NE-SW and the minimum  
338 principal stress ( $\sigma_3$ ) is close to vertical, outlining an overall compressional stress field; this accounts  
339 for approximately one third of the faults analysed (n=11), including several of the NE-dipping oblique  
340 (right-lateral) reverse faults (Fig. 8, green stereonet). A second stress field has  $\sigma_1$  horizontal E-W and  
341  $\sigma_3$  horizontal N-S (n = 10), and  $\sigma_3$  and  $\sigma_2$  are of similar magnitude. NE-dipping faults are also active  
342 within this stress field, but with a mixture of dip-slip reverse and left-lateral movement (Fig. 8, blue  
343 stereonet). A third stress field is also strike-slip, with near-vertical  $\sigma_2$ , NE-SW  $\sigma_3$  and NW-SE  $\sigma_1$ .  $\sigma_1$  and  
344  $\sigma_2$  are proposed to be of similar magnitude, so that the effect of  $\sigma_3$  may be dominant; faults with  
345 some extensional component are attributed to this stress field (n=7, orange stereonet, Fig. 8). Four  
346 more faults can be attributed to another strike-slip stress field where  $\sigma_1$  is WNW-ESE and  $\sigma_2$  is NNE-  
347 SSW (pink stereonet, Fig. 8). The stress ratio is similar to the strike-slip stress field with NE-SW  $\sigma_3$ .  
348 The fault attributed to this stress field are mostly oblique left-lateral extensional. A further five faults  
349 have large misfits to all of these palaeostress solutions and do not combine in enough numbers to  
350 suggest any further stress fields, and so remain unattributed (Fig. 8).

### 351 Stress fields from en-echelon injection veins

352 The orientation of en-echelon pseudotachylyte injection vein arrays are described by the  
353 trend of the perpendicular direction either to an individual en-echelon segment (the  
354 segment-normal), or to the overall vein array (the array-normal). Across the dataset, the

355 segment-normals have a dispersed range of orientations with no obvious modal trend (Fig.  
356 9a). However, they often lie within the range NW-SE to N-S (Fig. 9a). The array-normals have  
357 a modal NW-SE trend, but also show N-S and E-W opening directions (Fig. 9b).

358 Within any en-echelon array, the segment-normal typically deviates at some angle from the  
359 array-normal (Figs. 6c, 9c). The segment-normal may be found either clockwise and anti-  
360 clockwise from the array-normal in the OHFZ pseudotachylytes. These senses of deviation  
361 from the azimuth of the array-normal to that of the segment-normal are not restricted to  
362 any particular orientation range of the parent array, but for each sense there is a peak in the  
363 magnitude of deviation at a given azimuth of the array-normal (Fig. 9c). Typically, the  
364 segments have an azimuthal deviation of  $\leq 20^\circ$  from the parent array. For the clockwise sense,  
365 the maximum deviation is  $\sim 80^\circ$  and occurs where the array-normal is ESE-WNW. For the  
366 anti-clockwise sense, the maximum magnitude of deviation is  $\sim 50^\circ$  and occurs when the  
367 array-normal is ENE-WSW. In any single locality along the OHFZ region, similarly oriented  
368 en-echelon arrays may show opposite senses of azimuth deviation, and a variety of  
369 orientations exist (Fig. 10).

## 370 **Discussion**

371 Traditionally, the OHFZ has been considered as part of the Caledonian collisional system, due largely  
372 to the widespread development of thrust kinematics and the overall NNE-SSW strike and ESE dip-  
373 direction of the entire fault zone (Fig. 1), subparallel to the Moine Thrust on the Scottish mainland  
374 (Smythe et al., 1982; Streule et al., 2010). This idea influenced early names for the OHFZ, including  
375 'Outer Isles Thrust' (e.g. Coward, 1969; Sibson, 1975). However, the orientation of different  
376 segments of the OHFZ varies on the kilometre scale, with local strikes varying from N-S through to E-  
377 W (Fig. 1). Orientations of small length scale pseudotachylyte-bearing fault planes in the OHFZ are  
378 also varied, with a higher proportion of NE-dipping faults than the large-scale OHFZ fault trace might



379 suggest (Fig. 1). Pseudotachylyte-bearing faults, which record seismicity, include a spectrum of  
380 normal, reverse and strike-slip movement. The balance between reverse and normal faulting in  
381 particular has been much discussed in several studies of the OHFZ (e.g. White and Glasser, 1987;  
382 Osinski et al., 2001) and there are now a number of studies which recognise evidence for late  
383 Caledonian reactivation of the OHFZ with strike-slip and extensional kinematics (see Table 1).  
384 Pseudotachylyte-bearing normal faults in the OHFZ are sometimes suggested to have locally  
385 accommodated block movements during the major thrusting phase of the OHFZ (Butler, 1995).  
386 However, in southern portions of the onshore OHFZ, particularly in South Uist and Barra, kinematic  
387 evidence for extensional faulting is locally more widespread than reverse movement (White and  
388 Glasser, 1987; Osinski et al., 2001; see Table 1) and pseudotachylyte-bearing normal faults have  
389 been shown to form part of a distinct, relatively late phase of extension (MacInnes et al., 2000). The  
390 current study extends the discussion over the relative importance of the varying kinematics of fault  
391 slip, focussed mostly on the seismic behaviour recorded by the pseudotachylytes, but considers also  
392 the overall heterogeneity and temporal evolution in deformation behaviour on a long-lived and  
393 reactivated fault zone such as the OHFZ.

#### 394 Controls on fault orientation in the OHFZ

395 Amongst the variation in orientations of individual pseudotachylyte-bearing fault segments is a  
396 prominent NE-dipping set (Fig. 1). Slip direction analysis indicates that these NE-dipping faults  
397 accommodate a range of fault movements ranging from both left- and right- lateral strike-slip  
398 through to oblique dip-slip and some dominantly dip-slip reverse faults (Fig. 8). This significant  
399 number of NE-dipping faults accommodating slip within the OHFZ system, in contrast to the  
400 approximate ESE-dipping trend of the main OHFZ fault trace, might suggest some control by other  
401 structures on the orientation of fault formation. This could include reactivation of pre-existing fault  
402 planes, or involve fault initiation exploiting alternative localised weak structures such as foliation or

403 lithological boundaries within the country rock. We briefly evaluate the potential influence of such  
404 structures here.

405 Considering the first option, appropriate candidates for widespread pre-existent fault systems are  
406 difficult to pinpoint as both Laxfordian (e.g. South Harris Shear Zones) and post-Caledonian faults,  
407 whilst also striking NW-SE, are invariably steeper than the NE dipping pseudotachylyte-bearing faults  
408 (Fettes et al., 1992; MacInnes et al., 2000). Within the Lewisian Gneiss Complex that hosts the OHFZ,  
409 the most pervasive structure that could potentially have been exploited for slip is the foliation,  
410 generally formed by gneissic banding (Fettes and Mendum, 1987). The banding concentrates layers  
411 of minerals such as biotite and amphibole, which are likely to be mechanically and frictionally  
412 weaker relative to quartzo-feldspathic layers (Spray, 2010). Additionally, the lower melting  
413 temperatures of biotite and amphibole (Spray, 2010) may bias the generation of pseudotachylyte  
414 onto faults along biotite- or amphibole-rich layers. The foliation across the Outer Hebrides, excluding  
415 any mylonitic or cataclastic fabrics associated with the OHFZ, was regionally folded during pre-OHFZ  
416 Laxfordian deformation, but typically dips moderately to steeply NE or northwards (Fettes et al.,  
417 1992), similar to the pseudotachylyte-bearing faults (Fig. 1). However, pseudotachylyte generation  
418 planes are rarely truly parallel to the immediately adjacent foliation (Fig. 11), although brecciated  
419 faults in particular often lie at a low angle to it. Thus, the foliation does not appear to be exploited  
420 directly for fault initiation, which may indicate either a high angle between the foliation and the  
421 maximum compressive stress, or a large confining pressure (Tien et al., 2006). There is some  
422 indication, however, that strong foliation planes oriented between 15-75° from the maximum  
423 principal stress may facilitate a preferred orientation of shear fractures towards the foliation fabric  
424 (Donath, 1961, Tien et al., 2006). This may explain why so many of the faults lie at relatively low  
425 angles to the surrounding foliation, despite the suggested changes in stress field (Fig 8.) varying the  
426 orientation of  $\sigma_1$ .

427 If no exploitable pre-existing structures are available, new faults with more ideal orientations should  
428 instead form, responding to the variation in stress fields suggested by the fault slip analysis (Fig. 8).  
429 NE-dipping faults may have preferentially formed when  $\sigma_1$  or  $\sigma_3$  was oriented NE-SW, for example. In  
430 fact, the major fault structures of the OHFZ (as mapped in Fig. 1) are more likely to represent the  
431 reactivation of pre-existing and potentially misoriented structures (Imber et al., 2002) than the  
432 small, apparently single-slip faults that we consider here. One scenario could be that NE-SW  
433 compression featured as an early transpressional stress regime preceding Caledonian convergence  
434 (Fig. 12), and scattered seismicity reflected the lack of a large through-going fault zone (the OHFZ) at  
435 this stage.

436 Alternatively, it remains possible that some number of the pseudotachylyte faults may pre-date  
437 Caledonian movement on the main trace of the OHFZ, bearing in mind that some OHFZ  
438 pseudotachylytes can be related with good certainty to Caledonian movement (Sibson, 1977a, Kelley  
439 et al., 1994, MacInnes et al., 2000). Early pseudotachylyte, viscously deformed within mylonite  
440 sequences (Sibson, 1980, White, 1996), may relate to (or predate) the proposed early phase of  
441 generally ductile reverse movement along the OHFZ (Imber et al., 2002), and equivalent age faults  
442 may be preserved without a viscous overprint outside the main shear zone localities. However, this  
443 phase of early OHFZ compression is also thought to have been top-to-NW (Imber et al., 2002), so  
444 does not help account for the variation in pseudotachylyte orientations that we observe here. The  
445 age of earliest possible OHFZ movement is set at  $\sim 1.1$  Ga (Imber et al., 2002), constrained by the  
446 cessation of activity on the South Harris Shear Zones (Cliff & Rex, 1989). Earlier brittle faulting  
447 unrelated to the OHFZ is another possible scenario (Fig. 12); on mainland west-coast Scotland, 1.55  
448 Ga brittle faulting within in the Lewisian complex has been identified in the Canisp Shear Zone  
449 (Hardman, 2019) alongside 1.5 Ga faulting near the Loch Assynt Fault, both of which appear linked  
450 to a regional (Assyntian) strike-slip deformation event (Holdsworth et al., 2020). Later brittle faulting  
451 in the Gairloch Shear Zones relates to regional deformation at 0.98-1.12 Ga (Sherlock et al., 2008).  
452  $^{40}\text{Ar}$ - $^{39}\text{Ar}$  dating studies of the OHFZ pseudotachylytes do not particularly corroborate with any of

453 these regional events, but have confirmed that some of the OHFZ pseudotachylytes are of  
454 Caledonian age (Kelley et al., 1994) whilst some are likely older (Sherlock et al., 2009).

455 Although the OHFZ pseudotachylytes are typically inferred to result from tectonic faulting (Sibson,  
456 1975, MacInnes et al., 2000, Osinski et al., 2001, O'Callaghan & Osinski, 2019), an alternative  
457 explanation for some proportion of the widespread faulting across the Outer Hebrides is sometimes  
458 suggested to be impact cratering (Sherlock et al., 2009). Although no clear field or microstructural  
459 evidence for shock deformation has been found around the Outer Hebrides, there is mounting  
460 evidence that the 1.18 Ga Stac Fada Member of the Stoer Group, which crops out on the west-coast  
461 Scottish mainland, represents an ejecta deposit (Amor et al., 2008, Reddy et al., 2015). Transport  
462 direction indicators have promoted the idea that the impact site would likely sit offshore in the  
463 Minch Basin, between the mainland and the Outer Hebrides (Amor et al., 2019), and whilst this  
464 interpretation is contested (Simms, 2020), alternative impact sites have proved difficult to reconcile  
465 in terms of size and location (Simms and Ernstson, 2019). The proposed site lies ca. 40 km from  
466 Stornoway in eastern Lewis (see Fig. 14 of Amor et al., 2019). However, the relative positions of the  
467 Outer Hebrides and the Scottish mainland have been modified by significant fault movement since  
468 the impact date; although the sense and magnitude of such movement is not well constrained, it  
469 likely included significant (90 km) strike slip movement associated with the OHFZ and sub-Minch  
470 Basin faults (Piper, 1992, Whitehouse and Bridgewater, 2001), placing great uncertainty on the  
471 spatial association of the OHFZ pseudotachylytes with the proposed impact site. It also follows that it  
472 is difficult to predict the probable character and orientation of any impact-related pseudotachylytes;  
473 veins interpreted as shock features in the centre of the Vredefort Dome crater (South Africa) are  
474 characterised by small displacements, steep dips and a relatively random orientation (Dressler &  
475 Reimold, 2004), but more distal pseudotachylytes exposed in the Sudbury Crater (Canada) are  
476 related to frictional slip processes during crater collapse and reflect the crater geometry, forming  
477 large ring faults (Thompson & Spray, 1996). Evidence for shear movement associated with the OHFZ  
478 pseudotachylyte faults demonstrated in the current study may imply that, if any of these

479 pseudotachylytes were related to an impact event, they more likely relate to crater-related faulting,  
480 although the geometries of brecciation and injection are comparable with those exposed in  
481 Vredefort (Garde & Klausen, 2016). Whilst it is possible that some of the OHFZ pseudotachylytes  
482 were generated during an impact cratering event and do not represent a tectonic stress-field,  
483 significant numbers of pseudotachylyte faults across the Outer Hebrides remain likely to be tectonic.

484 *Slip directions and stress fields of ancient seismicity on the OHFZ: comparison of methods*

485 *Interpreting the stress field from en-echelon pseudotachylyte arrays: uncertainties*

486 Observations of en-echelon pseudotachylyte injection veins often lack constraint on the causative  
487 fault plane orientation, restricting a complete analysis of the stress field. According to the en-  
488 echelon model proposed above, however, the rotation of injection vein propagation trajectories to  
489 form en-echelon veins should provide some indication of the minimum principal stress direction  
490 even when the fault plane itself is not observed. In this model, en-echelon pseudotachylyte vein  
491 segments form by rotation of their propagation trajectory away from the initial orientation at the  
492 base of the injection vein, as the influence of the coseismic rupture-tip stress field wanes and a far-  
493 field tectonic stress field becomes the dominant control on tensile opening. However, in practice,  
494 analysis of the opening direction of the segments does not reveal clear trends (Fig. 9a). This may be  
495 because the segments either did not achieve the ideal angle of rotation during their propagation, or  
496 are not currently exposed at the level of their maximum azimuthal deviation, in order to align with  
497 the true direction of the far-field minimum compressive stress, or alternatively there are some  
498 invalid assumptions in this model. The extent of azimuthal deviation will depend on the difference  
499 in orientation between the dynamic rupture-tip and far-field stress fields, the distance the en-  
500 echelon segments have propagated from their origin at the fault vein, and at what level the plane of  
501 observation is along the length of the injection vein. The abundance of steeply dipping en-echelon  
502 segments may indicate that, for many of these seismic events, the far-field minimum compressive  
503 stress was close to horizontal. This implies that extensional and/or strike-slip stress regimes are

504 represented by these en-echelon arrays, in keeping with other evidence presented here for sets of  
505 extensional and strike-slip pseudotachylyte faults.

506 The greatest magnitude of azimuth deviation of the en-echelon segment trajectories from the  
507 parent array should occur when the array opening direction exhibits the most misorientation with  
508 respect to the minimum compressive stress direction. As the largest magnitudes of azimuth  
509 deviation are recorded when the array opening direction is between 080° and 110° (Fig. 9c), the  
510 direction of  $\sigma_3$  could be close to N-S. Under this stress field, where the maximum horizontal principal  
511 stress is consequentially approximately E-W, west- or easterly-dipping faults should show reverse  
512 movement, NE- or SW-dipping faults should show some element of left-lateral strike slip and NW- or  
513 SE-dipping faults, right lateral. Such configurations account for observations of left lateral strike-slip  
514 on NE dipping faults (Fig. 8). However, E- and W-dipping normal faults are better explained by  
515 rotating the minimum principal stress towards a more E-W trend. Thus, whilst the en-echelon data  
516 may not precisely define the directions of all three principal stresses, they do indicate that more  
517 than one stress field is necessary to explain the observed fault slip directions, in line with field  
518 observations of cross-cutting en-echelon vein arrays (Fig. 5a).

#### 519 *Interpreting the stress field from palaeostress analysis: uncertainties and sources of error*

520 The use of dynamic tensile injection veins to firstly reconstruct the orientation of slip and then to  
521 subsequently use those slip directions in palaeostress inversion is a novel approach, but it involves  
522 repeating stages of interpretation and analysis, potentially allowing the propagation of errors  
523 through to the resulting stress tensors. However, whilst errors in the slip direction identification will  
524 certainly lead to errors in the stress tensor orientation, these may only become significant when the  
525 error in the slip direction is  $>10^\circ$  (Žalohar & Vrebac, 2007).

526 Another source of uncertainty in the stress field interpretation is the relatively small dataset of fault  
527 orientations and slip directions, which leads to some stress tensor solutions being based on smaller  
528 than ideal fault populations (i.e.  $> 9$ , Orife & Lisle, 2006); also, the greater the number of stress

529 tensor solutions suggested, the more likely that each solution has a low number of faults attributed  
530 to it. In addition, the Gauss method used cannot distinguish stress tensors with  $< 10^\circ$  difference in  
531 the orientation of principal stresses, although it has greater resolution than other palaeostress  
532 methods (Žalohar & Vrebac, 2007). This prompts us to avoid the use of overly narrow subsets (see  
533 Supplementary Information); however, the resulting risk is that a best-fit stress tensor is produced  
534 that is not a reflection of any real stress field, but an amalgamation of several similar solutions. We  
535 additionally disregard stress tensor solutions output by the palaeostress analysis based on fault  
536 numbers below that which should be mathematically stable (i.e.  $n = 4$ , Etchecopar et al., 1981). One  
537 palaeostress solution has  $n = 4$  (pink stereonet, Fig. 8), and the weight we place on its interpretation  
538 is discussed below. If, as we suggest, the pseudotachylite faults represent long-lived seismic activity  
539 throughout progressive changes to the stress field, a large number of stress tensors showing  
540 progressive long-term rotation of the principal stresses might be the most realistic approximation.  
541 Nevertheless, the method still highlights clearly that no single stress field can explain all of the fault  
542 slip data.

543 A further source of uncertainty are the input parameters defined during palaeostress analysis. We  
544 have tested the results for sensitivity to varying these parameters within a reasonable range of  
545 values (Supp. Fig. 1 and accompanying text). If we vary the dispersion of angular misfit between the  
546 ideal and real slip direction, or the threshold for mechanical compatibility (see Supp. Info), the main  
547 differences in the stress tensor solutions are that there may be another dominantly compressional  
548 field where  $\sigma_1$  is NW-SE (i.e. a more typical 'Caledonian' shortening trend), or that the NE-SW  $\sigma_3$   
549 strike-slip stress field may be an extensional stress field. Otherwise, the results using various input  
550 parameters (Supp. Fig. 1) tend to be similar to those presented in Fig. 8.

551 The interpretation of palaeostress fields from fault slip inversion methods involves a number of  
552 general assumptions (e.g. Simón, 2018, and references therein): (i) that there can be no differential  
553 rotation between bodies of rock separated by faults; (ii) that there is no interaction between faults

554 or pre-existing anisotropy that controls the fault orientation and slip; (iii) that the volume of rock  
555 considered is much larger than the length scale of the faults; and (iv) that the faults are much larger  
556 than the scale of displacement. In the OHFZ, the pseudotachylite-bearing faults studied are small,  
557 typically less than ~10 m in length, and subsequently displacements are also small. Any slip-  
558 facilitated rotation across these faults is therefore expected to be minimal. Rotation of larger-scale  
559 fault blocks is worth greater consideration because the observations are taken from a large area that  
560 is subdivided by later faulting (Fettes et al., 1981). However, these late faults tend to be subvertical  
561 strike-slip faults (MacInnes et al., 2000) and are therefore unlikely to have induced significant  
562 differential rotation across the Outer Hebrides. The entire Outer Hebrides block, including the OHFZ,  
563 was likely uplifted and rotated as a footwall block during the Mesozoic initiation of the Minch Fault,  
564 and may have been rotated about a subhorizontal NE-SW axis by up to 15° towards the WNW  
565 (Roberts and Holdsworth, 1999). Such a rotation would have had the effect of steepening ESE- and  
566 easterly-dipping faults without inducing significant change to the principal stress directions  
567 calculated from present day fault orientations. Considering other assumptions of the fault slip  
568 analysis, interaction between faults in the OHFZ is difficult to interpret and, as previously discussed,  
569 fault orientation may have been influenced by the foliation. However, the volume scaling between  
570 overall volume, fault length and displacement is generally considered a valid assumption in this  
571 study.

#### 572 *Comparison of slip direction and stress field results*

573 Collating the results from each of the approaches used in this study (i.e. offset markers, en-echelon  
574 vein arrays and dynamic tensile injection veins) indicates that two slip directions, NW-SE (varying to  
575 WNW-ESE) and NE-SW (varying to NNE-SSW), appear to dominate. The stress field orientations  
576 necessary for these fault populations are most readily interpreted from palaeostress analysis on the  
577 dynamic injection vein observations, but these must corroborate with more tentative interpretations  
578 from the other approaches. Because datasets for each method of analysis are relatively small, there



579 is potential for results to be skewed by a small, unrepresentative input dataset. However, by  
580 comparing the independent datasets for each method, any such problem should be recognised. Both  
581 the en-echelon veins and the off-fault tensile injection vein analyses suggest that  $\sigma_3$  may have varied  
582 in orientation between east-west and north-south (or NE-SW) at different stages. This orientation  
583 for  $\sigma_3$  corresponds broadly to the two strike-slip stress fields suggested by fault slip analysis,  
584 although  $\sigma_3$  is not implied there to be exactly E-W (Fig. 8).

585 Another stress field suggested by palaeostress analysis is compressional, where  $\sigma_3$  is sub-vertical and  
586  $\sigma_1$  is NE-SW (Fig. 8). This stress field is seemingly not recorded in the en-echelon dataset, possibly  
587 because the majority of observed en-echelon veins are steeply dipping. A sub-vertical  $\sigma_3$  would  
588 ideally encourage injection veins to shallow as they propagated away from the generating fault, and  
589 this geometry may be less likely to be visible on the frequently near-horizontal exposures. The  
590 compressional field is considered unlikely to be an artefact for several reasons: firstly, due to the  
591 relatively large number of faults that are included in this field (11 out of a total 30 observations, Fig.  
592 8), and secondly, because the reverse NW-SE slip direction frequently recorded by both the field  
593 offset data (Fig. 7) and the tensile injection vein analysis can be partly attributed to this  
594 compressional field (Fig. 8). Compressional faulting in general is well documented across non-  
595 pseudotachylite-bearing faults and fault rocks in the OHFZ, although the inferred direction of  
596 compression tends to be NW-SE, parallel to the most typically observed slip directions (e.g. Sibson  
597 1977b, Fettes et al. 1992, Butler et al., 1995; MacInnes et al., 2000; Osinski et al., 2001; Imber et al.,  
598 2002, Ferré et al., 2016). Some combinations of the palaeostress analysis input parameters do  
599 suggest a stress field with NW-SE directed compression (Supp. Fig. 1), but always in addition to a NE-  
600 SW directed compressional field. One of the strike-slip stress fields (with E-W  $\sigma_1$ ) also accounts for  
601 NW-SE slip directions on faults with some reverse component (blue stereonet, Fig. 8). We do  
602 therefore do not rule out any period of NW-SE directed compression, but we interpret our results to  
603 suggest that a phase of NE-SW compression also occurred.

604 The NE-SW  $\sigma_3$  strike-slip stress field (orange stereonet, Fig. 8) is derived from a smaller number of  
605 faults (7 out of a total 30) showing mainly normal-component movement of varying obliquity (Fig. 8),  
606 with the fault planes dipping predominantly to the west and to the NE and slip directions to the  
607 north, ENE and SW. Most faults with a component of normal movement are incorporated in this  
608 field from the tensile injection vein dataset. In contrast, the offset marker data mostly show faults  
609 with apparent normal slip to dip towards the east, SE and to some extent NW to northwards (Fig. 7).  
610 It may be that a greater variety of normal-component faults exist than are included in the  
611 palaeostress analysis. This NE-SW  $\sigma_3$  stress field also lacks the optimum threshold number of faults  
612 for a stable analysis (9, Orife & Lisle, 2006), as does an additional stress field with NNE-SSW  $\sigma_1$  (pink  
613 stereonet, Fig. 8) that also incorporates extensional-component faults (though these are dominantly  
614 strike-slip), in this case with NNW-SSE slip vectors. Although proposed as a palaeostress solution, it  
615 has attributed to it a very small number of faults ( $n = 4$ , Fig. 8). For this reason we do not place any  
616 great weight on this additional stress field, except to consider that the similarity of the stress ratio  
617 and the simple rotation of  $\sigma_3$  and  $\sigma_1$  between this stress field and the strike-slip field where  $\sigma_3$  is NE-  
618 SW may imply that both are related and provide approximations of some progressive rotation.  
619 Despite the small fault numbers attributed to each of these stress fields in the fault slip analysis,  
620 faults with a normal component are not rare in the offset marker database (Fig. 7) and, in the west-  
621 and NE- dipping orientations suggested there, are unlikely to be mechanically attributable to the  
622 compressional and E-W  $\sigma_1$  strike-slip stress fields also suggested by the palaeostress analysis. Hence,  
623 we do expect that the majority of extensional pseudotachylyte-bearing faults relate to a separate  
624 stress field, even though the orientation of that stress tensor remains uncertain.

625 The stress field for each pseudotachylyte fault may be subject to local spatial or temporal variations,  
626 which means that the 'far-field stress' from the en-echelon analysis may not be equivalent to the  
627 regional tectonic-scale stress. This effect introduces some uncertainty into the stress tensor results  
628 from palaeostress analysis as well as some misfit of fault slip orientations in the population  
629 associated with each resulting tensor. These stress variations may be spatial, relating to changes in

630 orientation of the major fault structures of the OHFZ. Alternatively, there may be an additional  
631 temporal aspect, either spanning long-term changes as the fault network geometry evolves over  
632 time (Moir et al., 2010), or where local stresses change within seismic timescales, where the stress  
633 field is transiently perturbed by seismic activity on nearby fault segments (e.g. Das & Scholz, 1981,  
634 Nüchter & Ellis, 2011, Dempsey et al., 2014), including potentially within a single, complex rupture  
635 (e.g. as during the 2016 MW 7.8 Kaikoura earthquake., Hollingsworth et al., 2017). There is no  
636 obvious pattern of systematic changes in the stress field between different localities in the OHFZ  
637 (Figs. 8 & 10) that would indicate a purely spatial influence. Any localised temporal stress variation is  
638 also difficult to resolve from the general heterogeneity and the regional-scale change of stress field  
639 that we infer here. However, whilst it does not add enough uncertainty to alter our interpretation of  
640 ongoing seismicity during major changes to the stress field around the OHFZ, the potential for these  
641 local variations should be borne in mind when comparing individual faults, especially those situated  
642 significant distances apart.

643 There are few existing data on slip directions for seismic, pseudotachylyte-generating faults in the  
644 OHFZ with which to compare the slip direction results derived in this contribution. This is primarily  
645 due to the lack of markers from which to easily collect field observations. A recent anisotropy of  
646 magnetic susceptibility (AMS) analysis on an OHFZ pseudotachylyte sample from western South Uist  
647 interpreted top-to-the-WSW movement on an ENE dipping fault plane (Ferré et al., 2016), which fits  
648 with the data collected here for the subset of NE- and E- dipping reverse faults which would have  
649 had top-to-SW movement if predominantly dip-slip (Fig. 8). The lack of existing data means that the  
650 analyses presented here, whilst still limited in number by the availability of the appropriate field  
651 observations, remain a valuable attempt to further constrain both the seismic kinematics of the  
652 OHFZ and the general evolution of seismicity as long-lived fault zones reactivate under different  
653 kinematic conditions.

654 *Synthesis of stress fields for seismicity with the history of the OHFZ*

655 The framework of movement on the OHFZ within which to understand the context and potential  
656 timing of the results presented above has been previously established to some extent in the existing  
657 literature (Table 1). Whilst these new results for the kinematics of seismicity on the OHFZ fit into this  
658 framework, they also introduce additional evidence - primarily the recognition of a period where the  
659 maximum compressional stress was more NE-SW than NW-SE. In addition, the identification of  
660 dominantly extensional seismicity (producing pseudotachylyte) in a distinct kinematic phase of OHFZ  
661 activity increases the spatial extent of similar observations previously constrained to north Barra by  
662 MacInnes et al. (2002).

663 A phase of brittle reverse faulting in the OHFZ, dominantly top-to-NW, is usually attributed to  
664 Caledonian thrusting (e.g. Sibson, 1975, and others – see Table 1) and remains the major contender  
665 to explain NW-SE reverse movement on these ancient seismic faults. It should be noted, however,  
666 that an earlier top-to-NW kinematic phase around 1.1 Ga is also proposed for initiation of the OHFZ  
667 (Imber et al., 2002). Although this phase is assumed to involve deeper crustal viscous deformation,  
668 the presence of mylonitised pseudotachylytes in parts of the OHFZ (Sibson, 1980; White, 1996) and  
669 older  $^{40}\text{Ar}$ - $^{39}\text{Ar}$  dates from OHFZ pseudotachylytes (Sherlock et al., 2009) mean that a wider record of  
670 pre-Caledonian top-to-NW seismicity cannot be entirely ruled out. However, pseudotachylyte-  
671 bearing OHFZ faults in this study do not explicitly indicate that top-to-NW directed thrusting was the  
672 dominant component of seismic activity on the OHFZ. Whilst a NW-SE slip trend is apparent (Figs. 7,  
673 8, 9a), many of these faults are somewhat extensional, where the slip sense is known. Rather, the  
674 pseudotachylyte data suggest NE-SW compression, which is not only more difficult to match to  
675 known NW-SE or E-W shortening directions of mainland thrusting but also to other OHFZ reverse  
676 faults (Coward, 1969, 1983; Sibson, 1977b). However, the identified NE-SW trend of  $\sigma_1$  in this  
677 configuration could induce left lateral strike slip on SE- dipping faults, a kinematic phase observed in  
678 the OHFZ particularly on phyllonite shear zones (Butler et al., 1995; Imber et al., 1997).

679 In contrast, the strike-slip stress field predicted by the palaeostress analysis where  $\sigma_1$  is E-W has  
680 induced right lateral slip on SE-dipping faults (Fig. 8). The left-lateral strike slip reported by Butler et  
681 al. (1995) has been previously noted to be absent along some segments of the OHFZ, even where  
682 phyllonites are still present, especially towards the south of the fault zone in South Uist (Osinski et  
683 al., 2001) and Barra (MacInnes et al., 2000). Late Caledonian right-lateral strike slip faults with  
684 pseudotachylyte are reported by MacInnes et al. (2000) in Barra, alongside left-lateral equivalents.  
685 Our dataset also reports a mix of left- and right-lateral strike slip faults from several locations across  
686 the OHFZ, including western Barra, western South Uist, SE Lewis and west Lewis; some of these  
687 faults are attributed to the NE-SW compressional field and some of which are attributed to the E-W  
688  $\sigma_1$  strike-slip stress field (Fig. 8). It would be, therefore, an over-simplification to attribute all strike-  
689 slip faulting to the same late Caledonian strike slip phase as that recognised in the phyllonites (Butler  
690 et al., 1995). Our new data therefore add to the growing consensus that deformation mechanisms  
691 and kinematics along the OHFZ were highly variable across different segments (Butler et al., 1995,  
692 MacInnes et al., 2000, Osinski et al., 2001).

693 An extension-dominated regime of fault movement and seismicity is implied in our results (Fig. 8)  
694 and has been previously recognised across the OHFZ based on other field evidence, overprinting late  
695 Caledonian strike-slip deformation (Butler et al., 1995, MacInnes et al., 2000). A late Caledonian  
696 extensional phase is often included in discussion of the OHFZ's evolution, distinct to the later  
697 Mesozoic extensional phase that formed the North Minch and Sea of Hebrides basins to the east  
698 (Butler et al., 1995, MacInnes et al., 2000, Imber et al., 2001, Osinski et al., 2001, Szulc et al., 2008).  
699 The extensional faulting is associated with an overall strike-slip stress field in our palaeostress  
700 analysis, although with a similar magnitude of  $\sigma_2$  and  $\sigma_1$ , so that  $\sigma_3$  seems dominant (and indeed  
701 some combinations of input parameters suggest that this could be a true extensional stress field,  
702 Supp. Fig. 1). The extensional faults observed in this study are scattered around the OHFZ (Fig. 8),  
703 extending reports of significant Caledonian brittle normal faulting, including pseudotachylyte-  
704 bearing faults, from previous observations in North Uist, South Uist and Barra (White and Glasser,

705 1987, MacInnes et al., 2000, Osinski et al., 2001). As with all small faults, it is often difficult to date,  
706 even relatively, the movement(s) that they represent. Additionally, we do not have a sufficient  
707 number of observations of cross-cutting relationships on pseudotachylyte-bearing faults to  
708 meaningfully support our arguments. However, where these are found, evidence from cross-cutting  
709 pseudotachylytes reported in this study do illustrate that normal faulting (Figs. 3a-b) and/or a NE-SW  
710 minimum principal stress (Fig. 5a) were in some instances the later (or last) seismic event.

711 Our results also confirm that extensional seismic faulting on the OHFZ was largely a response to a  
712 separate kinematic regime, rather than localised accommodation or partitioning of deformation  
713 during an overall compression (MacInnes et al., 2000, Osinski et al., 2001). Although the trend of  $\sigma_3$   
714 is not confidently constrained, this variation in movement supports the observations of Osinski et al.  
715 (2001) on phyllonites and brittle normal faults along the North and South Uist sections of the OHFZ.

716 Overall, the slip directions and stress fields implied by our new dataset of pseudotachylyte-bearing,  
717 ancient seismic faults along the OHFZ fit with other field observations on brittle faults,  
718 pseudotachylyte-bearing faults and ductile shear zones (Table 1). They could support the proposed  
719 model of progressive transition from orogenic compression through oblique convergence to late  
720 extension-dominated tectonics to explain the kinematics of various segments of the OHFZ, possibly  
721 through the Caledonian orogenic event (MacInnes, 2000, Imber, 2001, Osinski, 2001). The relative  
722 scatter of pseudotachylyte-bearing faults illustrated here indicate that the stress fields inferred from  
723 fault slip analysis could be the result of a progressively rotating tectonic stress field (Lacombe, 2012)  
724 during which seismic behaviour was episodically active along several sections of the OHFZ. However,  
725 it should be noted that all the observations here, and in other field studies recording the kinematics  
726 of brittle faulting on the OHFZ (e.g. MacInnes et al., 2000, Osinski et al., 2001) consider dispersed  
727 faults <10 m in exposed length. This is in contrast to the major fault segments, for example the  
728 'crush zone' localities occurring in places such as Bealach an Easain, South Uist (Fig. 8) where  
729 faulting, fragmentation and chaotic cataclasite and pseudotachylyte networks makes clear

730 interpretations difficult, despite these being clearly important fault segments with significant fault  
731 displacement.

732 *Implications for long-lived reactivated crustal faults*

733 Continuous episodic seismicity through several kinematic phases of an orogen indicates that parts of  
734 a fault zone must remain strong and frictional, even if aseismic creep along weaker fault segments  
735 apparently accommodates some component of the far-field stress. Recognising this behaviour, and  
736 understanding where seismicity may nucleate, is important in the assessment of the seismic hazard  
737 along active faults, even where the likely magnitude of seismicity is small. Sections of the OHFZ have  
738 been used to illustrate how major reactivated fault zones weaken over time due to transformations  
739 to phyllosilicate-rich fault rocks and subsequent changes in deformation mechanisms (Imber et al.,  
740 1997). Comparisons have been made with processes occurring at depth along active fault zones such  
741 as the San Andreas (e.g. Holdsworth et al., 2011) and the Karakoram (Wallis et al., 2015). However, a  
742 growing body of evidence (including the current study) suggests that the OHFZ was highly  
743 heterogeneous along strike in terms of fault rock development, deformation mechanisms and  
744 accordingly fault strength for potentially much of its active history (MacInnes et al., 2000, Osinski et  
745 al., 2001). This is consistent with the identification in other exhumed fault zones of variable strength  
746 and structure evolution along different fault segments (Lawther et al., 2016), and multiple  
747 deformation mechanisms (Kirkpatrick & Shipton, 2009) including the identification of a coeval  
748 combination of periodic seismicity contemporaneous with ongoing aseismic creep along crustal scale  
749 faults at seismogenic depths (Edwards & Ratschbacher, 2005, Faulkner et al., 2008). Such complexity  
750 should therefore also be expected in present-day active fault zones. Understanding the fault  
751 structure and strength profile is hence important in assessing where earthquakes could nucleate.

752 The OHFZ provides a useful addition to the growing record of exhumed faults exhibiting mixed  
753 seismic slip and aseismic creep. In particular, the spatial scatter of seismicity away from the  
754 phyllonite belts provides an alternative geometrical model to that of interconnected networks of

755 weak aseismic material surrounding isolated seismic blocks (e.g. Faulkner et al., 2003, Fagereng &  
756 Sibson, 2010). The new dataset suggests that seismic faults were present along several sections of  
757 the fault zone during the strike-slip and extensional phases of the OHFZ, in regions both with and  
758 without major phyllonite-related fault weakening (Fig. 8). In the first case, dispersed seismicity  
759 feasibly represents episodic strain accommodation in the wall rock that cannot be localised into the  
760 weak deforming phyllonite fault zone, and perhaps maintains some strain compatibility between the  
761 weak phyllonite and the relatively strong wall rock, as is inferred adjacent to weak creeping faults  
762 elsewhere (e.g. Faulkner et al., 2003). In the case that the seismicity occurs along a fault segment  
763 lacking phyllonitic development (e.g. as detailed in MacInnes et al. 2000), the maximum rupture  
764 length is the size of the strong fault segment, whereas in the case that the seismicity occurs in strong  
765 wall rock near to phyllonite segments, the distributed faulting may be more fully characterised by  
766 small length scale ruptures with low moment magnitudes.

767 The general character of scattered seismicity across the OHFZ (Fig. 12), including several localities  
768 not generally considered to lie within the main fault zone (Figs. 1, 8), argues for a lack of localisation  
769 in basement faulting. Whilst the OHFZ is typically mapped as a single major fault trace, most  
770 continental thrust faults involve several major fault strands linked by smaller, but still potentially  
771 seismogenic, fault strands (e.g. Lin et al. 2011; Cheloni et al. 2016). It is likely that several small  
772 basins offshore west of the Outer Hebrides were formed by inversion of reverse faults parallel to,  
773 and probably coeval with, the main onshore trace of the OHFZ (Hitchen et al. 1995), and so the  
774 scattered pseudotachylytes may well be linked to a much wider fault system, of which the OHFZ is  
775 merely an onshore, exposed part. In addition, generation of pseudotachylyte along a fault tends to  
776 weld the fault plane and preclude further reactivation of that fault patch under brittle upper crustal  
777 conditions (Mitchell et al., 2016), encouraging delocalisation of seismicity. This relative strength of  
778 the fault and the host rock has been suggested by others (Faulkner et al., 2008, Lawther et al., 2016)  
779 to be a major control on whether faulting at seismogenic depths becomes localised or remains  
780 dispersed. The OHFZ supports this model as the pseudotachylyte-bearing faults generally do not



781 indicate reworking of earlier pseudotachylytes from the same fault plane; rather, they display  
782 clusters of adjacent pseudotachylyte faults, suggesting that forming a new slip plane was easier than  
783 re-rupturing an existing pseudotachylyte-bearing fault. This model is not only limited to fault zones  
784 where pseudotachylytes are present, but is also applicable where mineralisation strengthens the  
785 fault (Lawther et al., 2016), or where weak fault rocks form in the fault zone but the host rock is of a  
786 similar strength (Faulkner et al., 2008), or where a series of scattered precursor structures (typically  
787 joints in crystalline basement) are weaker than the faults that exploit them (Faulkner et al., 2008).  
788 Where this strength ratio is controlled by permeability, fluid flow and type of mineralisation, it may  
789 change over time in a series of strength cycles causing a set of fault segments to experience variable  
790 drive to become active or to switch off (Lawther et al., 2016). However, in the case of  
791 pseudotachylyte fault welding, the drive to remain dispersed is likely to continue even in relatively  
792 mature fault zones (c.f. Ben-Zion & Sammis, 2003).

793 Some of the small faults hosting pseudotachylyte away from the main fault zone could also  
794 represent aftershocks that might have been encouraged to nucleate in off-fault areas in response to,  
795 for example, Coulomb stress changes driven by seismicity on the main fault (Das and Scholz, 1981).  
796 Such a suite of aftershocks may record a range of slip modes and stress fields that are not  
797 representative of the mainshock (Schulz & Evans, 2000; Dempsey et al., 2014; Cheng et al., 2018)  
798 and could provide an alternative explanation for the variable nature of fault kinematics in the OHFZ.  
799 Nevertheless, the seismic hazard of aftershocks may still be high (e.g. Gorkha earthquake, May 2015,  
800 Avouac et al., 2015). Thus, the inclusion and understanding of off-fault seismicity in all forms of fault-  
801 zone study is crucial to understanding the stress field and energy release of large-scale fault zones  
802 (Ross et al., 2017; Cooke and Beyer, 2018).

### 803 **Conclusions**

804 Ancient seismic faults in the exhumed OHFZ, represented by pseudotachylyte-bearing fault planes,  
805 record a range of slip directions for the fault zone, suggesting that seismicity involved the full

806 spectrum of reverse, normal and strike-slip fault movements. In part, this relates to variation in fault  
807 plane orientations, which diverge from the average ESE-dip direction of the large-scale OHFZ. Whilst  
808 the typical Caledonian thrusting traditionally attributed to the OHFZ pseudotachylytes has a NW-SE  
809 slip trend, the pseudotachylyte faults considered here suggest an additional NE-SW slip trend and  $\sigma_1$   
810 direction for a compressional stress field. The pseudotachylytes record that seismicity was related to  
811 multiple kinematic regimes, and could potentially represent the continuation of seismicity through  
812 progressively oblique Caledonian convergence, strike-slip and late Caledonian extension. Even if  
813 some of the pseudotachylytes were generated outside of the Caledonian, ongoing seismicity over  
814 multiple tectonic regimes implies that segments of the major faults may remain frictionally strong  
815 through episodes of repeated activation, despite the evolution to weak deformation mechanisms  
816 along some portions of the fault.

817

#### 818 Acknowledgements

819 LC gratefully acknowledges funding from NERC (Studentship 1228272) and a National Museums  
820 Scotland CASE award that facilitated this work. Harri Wyn Williams is thanked for help with sample  
821 preparation and Richard Walshaw for SEM support at the Leeds Electron Microscopy and  
822 Spectroscopy Centre. T-TECTO software was funded by Quantectum AG, and by the Slovenian  
823 Research Agency (ARRS), the Republic of Slovenia, research project 1555-007-P1-0195. Zoe Shipton  
824 and an anonymous reviewer are thanked for their comments on this manuscript, which has greatly  
825 improved the work.

826

#### 827 References

828 Alneasan, M., Behnia, M. & Bagherpour, R. 2020. The effect of Poisson's ratio on the creation of  
829 tensile branches around dynamic faults. *Journal of Structural Geology*, 131, 103950,  
830 <https://doi.org/https://doi.org/10.1016/j.jsg.2019.103950>.

- 831 Amor, K., Hesselbo, S.P., Porcelli, D., Thackrey, S. & Parnell, J. 2008. A Precambrian proximal ejecta  
832 blanket from Scotland. *Geology*, 36, 303–306, <https://doi.org/10.1130/g24454a.1>.
- 833 Amor, K., Hesselbo, S.P., et al. 2019. The Mesoproterozoic Stac Fada proximal ejecta  
834 blanket, NW Scotland: constraints on crater location from field observations,  
835 anisotropy of magnetic susceptibility, petrography and geochemistry. *Journal of the  
836 Geological Society*, 176, 830 LP – 846, <https://doi.org/10.1144/jgs2018-093>.
- 837 Angelier, J. 1994. Fault slip analysis and paleostress reconstruction. In: Hancock, P. (ed.) *Continental  
838 Deformation*. New York, Pergamon, 53–100.
- 839 Avouac, J.-P., Meng, L., Wei, S., Wang, T., Ampuero, J.-P., 2015. Lower edge of locked Main  
840 Himalayan Thrust unzipped by the 2015 Gorkha earthquake. *Nature Geoscience* 8, 708.
- 841 Beach, A., 1975. The geometry of en-echelon vein arrays. *Tectonophysics* 28, 245–263.  
842 [https://doi.org/https://doi.org/10.1016/0040-1951\(75\)90040-2](https://doi.org/https://doi.org/10.1016/0040-1951(75)90040-2)
- 843 Behr, W.M., Platt, J.P., 2014. Brittle faults are weak, yet the ductile middle crust is strong:  
844 Implications for lithospheric mechanics. *Geophysical Research Letters* 41, 2014GL061349.  
845 <https://doi.org/10.1002/2014gl061349>
- 846 Ben-Zion, Y. & Sammis, C.G. 2003. Characterization of Fault Zones. *Pure and Applied Geophysics*,  
847 160, 677–715, <https://doi.org/10.1007/PL00012554>.
- 848 Bott, M.H.P., 1959. The Mechanics of Oblique Slip Faulting. *Geological Magazine* 96, 109–117.  
849 <https://doi.org/DOI:10.1017/S0016756800059987>
- 850 Brewer, J.A., Smythe, D.K., 1986. Deep structure of the foreland to the Caledonian Orogen, NW  
851 Scotland: Results of the Birps Winch Profile. *Tectonics* 5, 171–194.  
852 <https://doi.org/10.1029/TC005i002p00171>
- 853 Butler, C.A., 1995. Basement fault reactivation: The kinematic evolution of the Outer Hebrides Fault  
854 Zone, Scotland. Durham University.
- 855 Butler, C.A., Holdsworth, R.E., Strachan, R.A., 1995. Evidence for Caledonian sinistral strike-slip  
856 motion and associated fault zone weakening, Outer Hebrides Fault Zone, NW Scotland. *Journal  
857 of the Geological Society* 152, 743–746. <https://doi.org/10.1144/gsjgs.152.5.0743>
- 858 Campbell, L.R., Phillips, R.J., Walcott, R.C. & Lloyd, G.E. 2019. Rupture geometries in anisotropic  
859 amphibolite recorded by pseudotachylytes in the Gairloch Shear Zone, NW Scotland. *Scottish  
860 Journal of Geology*, 55, sjg2019-003, <https://doi.org/10.1144/sjg2019-003>.
- 861 Cheloni, D., Giuliani, R., et al. 2016. New insights into fault activation and stress transfer between en-  
862 echelon thrusts: The 2012 Emilia, Northern Italy, earthquake sequence. *Journal of Geophysical  
863 Research: Solid Earth*, 121, 4742–4766, <https://doi.org/10.1002/2016JB012823>.
- 864 Cheng, Y., Ross, Z.E., Ben-Zion, Y., 2018. Diverse Volumetric Faulting Patterns in the San Jacinto Fault  
865 Zone. *Journal of Geophysical Research: Solid Earth* 123, 5068–5081.  
866 <https://doi.org/10.1029/2017JB015408>

867 Clarke, G.L. & Norman, A.R. 1993. Generation of pseudotachylite under granulite facies  
868 conditions, and its preservation during cooling. *Journal of Metamorphic Geology*, 11,  
869 319–335, <https://doi.org/10.1111/j.1525-1314.1993.tb00151.x>.

870 Clemente, C.S., Amorós, E.B., Crespo, M.G., 2007. Dike intrusion under shear stress: Effects on  
871 magnetic and vesicle fabrics in dikes from rift zones of Tenerife (Canary Islands). *Journal of*  
872 *Structural Geology* 29, 1931–1942. <https://doi.org/http://dx.doi.org/10.1016/j.jsg.2007.08.005>

873 Cliff, R.A., Rex, D.C., 1989. Short Paper: Evidence for a ‘Grenville’ event in the Lewisian of the  
874 northern Outer Hebrides. *Journal of the Geological Society* 146, 921–924.  
875 <https://doi.org/10.1144/gsjgs.146.6.0921>

876 Collettini, C., Niemeijer, A., Viti, C., Marone, C., 2009. Fault zone fabric and fault weakness. *Nature*  
877 462, 907–910.

878 Cooke, M.L., Beyer, J.L., 2018. Off-Fault Focal Mechanisms Not Representative of Interseismic Fault  
879 Loading Suggest Deep Creep on the Northern San Jacinto Fault. *Geophysical Research Letters*  
880 45, 8976–8984. <https://doi.org/10.1029/2018GL078932>

881 Cowan, D.S., 1999. Do faults preserve a record of seismic slip? A field geologist’s opinion. *Journal of*  
882 *Structural Geology* 21, 995–1001. [https://doi.org/10.1016/S0191-8141\(99\)00046-2](https://doi.org/10.1016/S0191-8141(99)00046-2)

883 Coward, M.P., 1983. The thrust and shear zones of the Moine thrust zone and the NW Scottish  
884 Caledonides. *Journal of the Geological Society* 140, 795–811.  
885 <https://doi.org/10.1144/gsjgs.140.5.0795>

886 Coward, M.P., 1969. The structural and metamorphic geology of South Uist, Outer Hebrides.  
887 University of London.

888 Dalguer, L.A., Irikura, K., Riera, J.D., 2003. Simulation of tensile crack generation by three-  
889 dimensional dynamic shear rupture propagation during an earthquake. *Journal of Geophysical*  
890 *Research: Solid Earth* 108, 2144. <https://doi.org/10.1029/2001JB001738>

891 Das, S., Scholz, C.H., 1981. Off-fault aftershock clusters caused by shear stress increase? *Bulletin of*  
892 *the Seismological Society of America* 71, 1669–1675.

893 Dempsey, E.D., Holdsworth, R.E., Imber, J., Bistacchi, A., Di Toro, G., 2014. A geological explanation  
894 for intraplate earthquake clustering complexity: The zeolite-bearing fault/fracture networks in  
895 the Adamello Massif (Southern Italian Alps). *Journal of Structural Geology* 66, 58–74.  
896 <https://doi.org/http://dx.doi.org/10.1016/j.jsg.2014.04.009>

897 Di Toro, G., Nielsen, S., Pennacchioni, G., 2005. Earthquake rupture dynamics frozen in exhumed  
898 ancient faults. *Nature* 436, 1009–1012.  
899 [https://doi.org/http://www.nature.com/nature/journal/v436/n7053/supinfo/nature03910\\_S](https://doi.org/http://www.nature.com/nature/journal/v436/n7053/supinfo/nature03910_S)  
900 1.html

901 Donath, F.A., 1961. Experimental study of shear failure in anisotropic rocks. *Geological Society of*  
902 *America Bulletin* 72, 985–989. [https://doi.org/10.1130/0016-](https://doi.org/10.1130/0016-7606(1961)72[985:ESOSFI]2.0.CO;2)  
903 [7606\(1961\)72\[985:ESOSFI\]2.0.CO;2](https://doi.org/10.1130/0016-7606(1961)72[985:ESOSFI]2.0.CO;2)

904 Dressler, B.O. & Reimold, W.U. 2004. Order or chaos? Origin and mode of emplacement of breccias  
905 in floors of large impact structures. *Earth-Science Reviews*, 67, 1–54,  
906 <https://doi.org/https://doi.org/10.1016/j.earscirev.2004.01.007>.

- 907 Edwards, M.A. & Ratschbacher, L. 2005. Seismic and aseismic weakening effects in  
908 transtension: field and microstructural observations on the mechanics and architecture  
909 of a large fault zone in SE Tibet. Geological Society, London, Special Publications, 245,  
910 109 LP – 141, <https://doi.org/10.1144/GSL.SP.2005.245.01.06>.
- 911 Etchecopar, A., Vasseur, G. & Daignieres, M. 1981. An inverse problem in microtectonics for the  
912 determination of stress tensors from fault striation analysis. *Journal of Structural Geology*, 3,  
913 51–65, [https://doi.org/https://doi.org/10.1016/0191-8141\(81\)90056-0](https://doi.org/https://doi.org/10.1016/0191-8141(81)90056-0).
- 914 Fagereng, Å. & Sibson, R.H. 2010. Mélange rheology and seismic style. *Geology*, 38, 751–754,  
915 <https://doi.org/10.1130/G30868.1>.
- 916 Faulkner, D.R., Lewis, A.C. & Rutter, E.H. 2003. On the internal structure and mechanics of large  
917 strike-slip fault zones: field observations of the Carboneras fault in southeastern Spain.  
918 *Tectonophysics*, 367, 235–251, [https://doi.org/https://doi.org/10.1016/S0040-1951\(03\)00134-](https://doi.org/https://doi.org/10.1016/S0040-1951(03)00134-3)  
919 3.
- 920 Faulkner, D.R., Mitchell, T.M., Rutter, E.H. & Cembrano, J. 2008. On the structure and  
921 mechanical properties of large strike-slip faults. Geological Society, London, Special  
922 Publications, 299, 139 LP – 150, <https://doi.org/10.1144/SP299.9>.
- 923 Ferré, E.C., Yeh, E.-C., Chou, Y.-M., Kuo, R.L., Chu, H.-T. & Korren, C.S. 2016. Brushlines in fault  
924 pseudotachylytes: A new criterion for coseismic slip direction. *Geology*, 44, 395–398,  
925 <https://doi.org/10.1130/G37751.1>.
- 926 Ferré, E.C., Chou, Y.-M., Kuo, R.L., Yeh, E.-C., Leibovitz, N.R., Meado, A.L., Campbell, L., Geissman,  
927 J.W., 2016. Deciphering viscous flow of frictional melts with the mini-AMS method. *Journal of*  
928 *Structural Geology* 90, 15–26. <https://doi.org/http://dx.doi.org/10.1016/j.jsg.2016.07.002>
- 929 Fettes, D.J., Mendum, J.R., 1987. The evolution of the Lewisian complex in the Outer Hebrides.  
930 Geological Society, London, Special Publications 27, 27–44.  
931 <https://doi.org/10.1144/gsl.sp.1987.027.01.04>
- 932 Fettes, D.J., Mendum, J.R., Smith, D.I., Watson, J., 1981. 1:100 000 geological sheets (Solid): Lewis  
933 and Harris, Uist and Barra. London.
- 934 Fettes, D.J., Mendum, J.R., Smith, D.I., Watson, J. V, 1992. *Geology of the Outer Hebrides: memoir*  
935 *for 1:100 000 geological sheets, Lewis and Harris, Uist and Barra.* HMSO, London.
- 936 Francis, P.W., Sibson, R.H., 1973. The Outer Hebrides Thrust. In: Park, R.G., Tarney, J. (Eds.), *The*  
937 *Early Precambrian of Scotland and Related Rocks of Greenland.* University of Keele, Keele, 95–  
938 104.
- 939 Garde, A.A. and Klausen, M.B., 2016. A centennial reappraisal of the Vredefort pseudotachylytes:  
940 shaken, not stirred by meteorite impact. *Journal of the Geological Society*, 173, 954–965.
- 941 Griffith, W.A., Rosakis, A., Pollard, D.D., Ko, C.W., 2009. Dynamic rupture experiments elucidate  
942 tensile crack development during propagating earthquake ruptures. *Geology* 37, 795–798.  
943 <https://doi.org/10.1130/G30064A.1>

- 944 Gupta, S., Cowie, P.A., Dawers, N.H., Underhill, J.R., 1998. A mechanism to explain rift-basin  
945 subsidence and stratigraphic patterns through fault-array evolution. *Geology* 26, 595–598.  
946 [https://doi.org/10.1130/0091-7613\(1998\)026<0595:AMTERB>2.3.CO;2](https://doi.org/10.1130/0091-7613(1998)026<0595:AMTERB>2.3.CO;2)
- 947 Hardman, K. 2019. Cracking Canisp: Deep void evolution during ancient  
948 earthquakes. *Geoscientist*, 29, 10–15, <https://doi.org/10.1144/geosci2019-003>
- 949 Hirose, T., & Shimamoto, T. (2005). Slip-Weakening Distance of Faults during Frictional Melting as  
950 Inferred from Experimental and Natural Pseudotachylytes. *Bulletin of the Seismological Society*  
951 *of America*, 95(5), 1666–1673. <https://doi.org/10.1785/0120040131>
- 952
- 953 Hitchen, K., Stoker, M.S., Evans, D. & Beddoe-Stephens, B. 1995. Permo-Triassic sedimentary and  
954 volcanic rocks in basins to the north and west of Scotland. Geological Society, London, Special  
955 Publications, 91, 87–102, <https://doi.org/10.1144/GSL.SP.1995.091.01.05>.
- 956 Hoek, J.D., 1991. A classification of dyke-fracture geometry with examples from Precambrian dyke  
957 swarms in the Vestfold Hills, Antarctica. *Geologische Rundschau* 80, 233–248.  
958 <https://doi.org/10.1007/bf01829363>
- 959 Holdsworth, R.E., Selby, D., Dempsey, E., Scott, L., Hardman, K., Fallick, A.E. & Bullock, R. 2020. The  
960 nature and age of Mesoproterozoic strike-slip faulting based on Re–Os geochronology of  
961 syntectonic copper mineralization, Assynt Terrane, NW Scotland. *Journal of the Geological*  
962 *Society*, jgs2020-011, <https://doi.org/10.1144/jgs2020-011>.
- 963 Holdsworth, R.E., van Diggelen, E.W.E., Spiers, C.J., de Bresser, J.H.P., Walker, R.J., Bowen, L., 2011.  
964 Fault rocks from the SAFOD core samples: Implications for weakening at shallow depths along  
965 the San Andreas Fault, California. *Journal of Structural Geology* 33, 132–144.  
966 <https://doi.org/https://doi.org/10.1016/j.jsg.2010.11.010>
- 967 Hollingsworth, J., Ye, L. & Avouac, J.-P. 2017. Dynamically triggered slip on a splay fault in  
968 the Mw 7.8, 2016 Kaikoura (New Zealand) earthquake. *Geophysical Research Letters*,  
969 44, 3517–3525, <https://doi.org/10.1002/2016GL072228>.
- 970 Imber, J., Holdsworth, R.E., Butler, C.A., Lloyd, G.E., 1997. Fault-zone weakening processes along the  
971 reactivated Outer Hebrides Fault Zone, Scotland. *Journal of the Geological Society* 154, 105–  
972 109. <https://doi.org/10.1144/gsjgs.154.1.0105>
- 973 Imber, J., Holdsworth, R.E., Butler, C.A., Strachan, R.A., 2001. A reappraisal of the Sibson-Scholz fault  
974 zone model: The nature of the frictional to viscous (“brittle-ductile”) transition along a long-  
975 lived, crustal-scale fault, Outer Hebrides, Scotland. *Tectonics* 20, 601–624.  
976 <https://doi.org/10.1029/2000tc001250>
- 977 Imber, J., Strachan, R.A., Holdsworth, R.E., Butler, C.A., 2002. The initiation and early tectonic  
978 significance of the Outer Hebrides Fault Zone, Scotland. *Geological Magazine* 139, 609–619.  
979 <https://doi.org/10.1017/s0016756802006969>
- 980 Kelley, S.P., Reddy, S.M., Maddock, R., 1994. Laser-probe <sup>40</sup>Ar/<sup>39</sup>Ar investigation of a  
981 pseudotachylyte and its host rock from the Outer Isles thrust, Scotland. *Geology* 22, 443–446.

- 982 [https://doi.org/10.1130/0091-7613\(1994\)022<0443:lpaao>2.3.co;2](https://doi.org/10.1130/0091-7613(1994)022<0443:lpaao>2.3.co;2)
- 983 Kirkpatrick, J.D. & Shipton, Z.K. 2009. Geologic evidence for multiple slip weakening  
984 mechanisms during seismic slip in crystalline rock. *J. Geophys. Res.*, 114, B12401,  
985 <https://doi.org/10.1029/2008jb006037>.
- 986 Krabbendam, M., Ramsay, J.G., Leslie, A.G., Tanner, P.W.G., Dietrich, D. & Goodenough, K.M. 2017.  
987 Caledonian and Knoydartian overprinting of a Grenvillian inlier and the enclosing Morar Group  
988 rocks: structural evolution of the Precambrian Proto-Moine Nappe, Glenelg, NW Scotland.  
989 *Scottish Journal of Geology*, 54, 13–35, <https://doi.org/10.1144/sjg2017-006>.
- 990 Lacombe, O., 2012. Do fault slip data inversions actually yield “paleostresses” that can be compared  
991 with contemporary stresses? *Comptes Rendus Geoscience* 344, 159–173.  
992 <https://doi.org/https://doi.org/10.1016/j.crte.2012.01.006>
- 993 Lawther, S.E.M., Dempster, T.J., Shipton, Z.K. & Boyce, A.J. 2016. Effective crustal  
994 permeability controls fault evolution: An integrated structural, mineralogical and  
995 isotopic study in granitic gneiss, Monte Rosa, northern Italy. *Tectonophysics*, 690, 160–  
996 173, <https://doi.org/https://doi.org/10.1016/j.tecto.2016.07.010>.
- 997 Legros, F., Cantagrel, J. & Devouard, B. 2000. Pseudotachylite (Frictionite) at the Base of the  
998 Arequipa Volcanic Landslide Deposit (Peru): Implications for Emplacement Mechanisms. *The*  
999 *Journal of Geology*, 108, 601–611, <https://doi.org/10.1086/314421>.
- 1000 Lieger, D., Riller, U., & Gibson, R. L. (2009). Generation of fragment-rich pseudotachylite bodies  
1001 during central uplift formation in the Vredefort impact structure, South Africa. *Earth and*  
1002 *Planetary Science Letters*, 279(1–2), 53–64.  
1003 <https://doi.org/http://dx.doi.org/10.1016/j.epsl.2008.12.031>
- 1004 Lin, J., Stein, R.S., Meghraoui, M., Toda, S., Ayadi, A., Dorbath, C. & Belabbes, S. 2011. Stress transfer  
1005 among en-echelon and opposing thrusts and tear faults: Triggering caused by the 2003 M<sub>w</sub> =  
1006 6.9 Zemmouri, Algeria, earthquake. *Journal of Geophysical Research*, 116, B03305,  
1007 <https://doi.org/10.1029/2010JB007654>.
- 1008 Lisle, R.J., 2013. Shear zone deformation determined from sigmoidal tension gashes. *Journal of*  
1009 *Structural Geology* 50, 35–43. <https://doi.org/https://doi.org/10.1016/j.jsg.2012.08.002>
- 1010 Macaudière, J., Brown, W.L., 1982. Transcrystalline shear fracturing and pseudotachylite generation  
1011 in a meta-anorthosite (Harris, Scotland). *Journal of Structural Geology* 4, 395–406.  
1012 [https://doi.org/10.1016/0191-8141\(82\)90031-1](https://doi.org/10.1016/0191-8141(82)90031-1)
- 1013 MacInnes, E.A., Alsop, G.I., Oliver, G.J.H., 2000. Contrasting modes of reactivation in the Outer  
1014 Hebrides Fault Zone, northern Barra, Scotland. *Journal of the Geological Society* 157, 1009–  
1015 1017. <https://doi.org/10.1144/jgs.157.5.1009>
- 1016 Maddock, R.H., 1983. Melt origin of fault-generated pseudotachylites demonstrated by textures.  
1017 *Geology* 11, 105–108. [https://doi.org/10.1130/0091-7613\(1983\)11<105:moofpd>2.0.co;2](https://doi.org/10.1130/0091-7613(1983)11<105:moofpd>2.0.co;2)
- 1018 Marrett, R., Allmendinger, R.W., 1990. Kinematic analysis of fault-slip data. *Journal of Structural*

- 1019           Geology 12, 973–986. [https://doi.org/10.1016/0191-8141\(90\)90093-E](https://doi.org/10.1016/0191-8141(90)90093-E)
- 1020   McCoss, A. M. (1986). Simple constructions for deformation in transpression/transension zones.  
1021           Journal of Structural Geology, 8(6), 715–718. [https://doi.org/https://doi.org/10.1016/0191-](https://doi.org/https://doi.org/10.1016/0191-8141(86)90077-5)  
1022           8141(86)90077-5
- 1023   Mitchell, T.M., Toy, V., Di Toro, G., Renner, J., Sibson, R.H., 2016. Fault welding by pseudotachylyte  
1024           formation. Geology . <https://doi.org/10.1130/G38373.1>
- 1025   Mohr-Westheide, T. & Reimold, W.U. 2011. Formation of pseudotachylitic breccias in the  
1026           central uplifts of very large impact structures: Scaling the melt formation. Meteoritics &  
1027           Planetary Science, 46, 543–555, <https://doi.org/10.1111/j.1945-5100.2011.01173.x>.
- 1028   Moir, H., Lunn, R.J., Shipton, Z.K. & Kirkpatrick, J.D. 2010. Simulating brittle fault evolution from  
1029           networks of pre-existing joints within crystalline rock. Journal of Structural Geology, 32, 1742–  
1030           1753, <https://doi.org/https://doi.org/10.1016/j.jsg.2009.08.016>.
- 1031   Nemcok, M., Lisle, R.J., 1995. A stress inversion procedure for polyphase fault/slip data sets. Journal  
1032           of Structural Geology 17, 1445–1453. [https://doi.org/https://doi.org/10.1016/0191-](https://doi.org/https://doi.org/10.1016/0191-8141(95)00040-K)  
1033           8141(95)00040-K
- 1034   Ngo, D., Huang, Y., Rosakis, A., Griffith, W.A., Pollard, D., 2012. Off-fault tensile cracks: A link  
1035           between geological fault observations, lab experiments, and dynamic rupture models. Journal  
1036           of Geophysical Research: Solid Earth 117, B01307. <https://doi.org/10.1029/2011jb008577>
- 1037   Nicholson, R., Pollard, D.D., 1985. Dilation and linkage of echelon cracks. Journal of Structural  
1038           Geology 7, 583–590. [https://doi.org/https://doi.org/10.1016/0191-8141\(85\)90030-6](https://doi.org/https://doi.org/10.1016/0191-8141(85)90030-6)
- 1039   Nicol, A., Walsh, J.J., Watterson, J., Underhill, J.R., 1997. Displacement rates of normal faults. Nature  
1040           390, 157–159.
- 1041   Nielsen, S., Mosca, P., Giberti, G., Di Toro, G., Hirose, T., & Shimamoto, T. (2010). On the transient  
1042           behavior of frictional melt during seismic slip. Journal of Geophysical Research, 115(B10),  
1043           B10301. <https://doi.org/10.1029/2009JB007020>
- 1044
- 1045   Nüchter, J.-A. & Ellis, S. 2011. Mid-crustal controls on episodic stress-field rotation around major  
1046           reverse, normal and strike-slip faults. Geological Society, London, Special Publications, 359,  
1047           187–201, <https://doi.org/10.1144/sp359.11>.
- 1048   O’Callaghan, J.W. & Osinski, G.R. 2019. Geochemical and petrographic variations in pseudotachylyte  
1049           along the Outer Hebrides Fault Zone, Scotland. Journal of the Geological Society, 177, 50–65,  
1050           <https://doi.org/10.1144/jgs2019-009>.
- 1051   Olson, J.E., Pollard, D.D., 1991. The initiation and growth of en échelon veins. Journal of Structural  
1052           Geology 13, 595–608. [https://doi.org/https://doi.org/10.1016/0191-8141\(91\)90046-L](https://doi.org/https://doi.org/10.1016/0191-8141(91)90046-L)
- 1053   Orife, T., Lisle, R.J., 2006. Assessing the statistical significance of palaeostress estimates: simulations  
1054           using random fault-slips. Journal of Structural Geology 28, 952–956.



- 1055 <https://doi.org/https://doi.org/10.1016/j.jsg.2006.03.005>
- 1056 Osinski, G.R., I, A.G., Oliver, G.J.H., 2001. Extensional tectonics of the Outer Hebrides Fault Zone,  
1057 South Uist, northwest Scotland. *Geological Magazine* 138, 325–344.
- 1058 Philpotts, A.R., 1964. Origin of pseudotachylites. *American Journal of Science* 262, 1008–1035.  
1059 <https://doi.org/10.2475/ajs.262.8.1008>
- 1060 Piper, J.D.A. 1992. Post-Laxfordian magnetic imprint in the Lewisian metamorphic complex  
1061 and strike-slip motion in the Minches, NW Scotland. *Journal of the Geological Society*,  
1062 149, 127–137, <https://doi.org/10.1144/gsjgs.149.1.0127>.
- 1063 Pollard, D.D., Segall, P., Delaney, P.T., 1982. Formation and interpretation of dilatant echelon cracks.  
1064 *Geological Society of America Bulletin* 93, 1291–1303. [https://doi.org/10.1130/0016-  
1065 7606\(1982\)93<1291:FAIODE>2.0.CO;2](https://doi.org/10.1130/0016-7606(1982)93<1291:FAIODE>2.0.CO;2)
- 1066 Reddy, S.M., Johnson, T.E., Fischer, S., Rickard, W.D.A. & Taylor, R.J.M. 2015. Precambrian reidite  
1067 discovered in shocked zircon from the Stac Fada impactite, Scotland. *Geology*, 43, 899–902.
- 1068 Rickard, M.J., Rixon, L.K., 1983. Stress configurations in conjugate quartz-vein arrays. *Journal of*  
1069 *Structural Geology* 5, 573–578. [https://doi.org/http://dx.doi.org/10.1016/0191-  
1070 8141\(83\)90069-X](https://doi.org/http://dx.doi.org/10.1016/0191-8141(83)90069-X)
- 1071 Roberts, A.M., Holdsworth, R.E., 1999. Linking onshore and offshore structures: Mesozoic extension  
1072 in the Scottish Highlands. *Journal of the Geological Society* 156, 1061–1064.
- 1073 Ross, Z.E., Hauksson, E., Ben-Zion, Y., 2017. Abundant off-fault seismicity and orthogonal structures  
1074 in the San Jacinto fault zone. *Science Advances* 3.
- 1075 Rowe, C.D., Griffith, W.A., 2015. Do faults preserve a record of seismic slip: A second opinion.  
1076 *Journal of Structural Geology* 78, 1–26.  
1077 <https://doi.org/http://dx.doi.org/10.1016/j.jsg.2015.06.006>
- 1078 Rowe, C.D., Ross, C., et al. 2018. Geometric Complexity of Earthquake Rupture Surfaces Preserved in  
1079 Pseudotachylite Networks. *Journal of Geophysical Research: Solid Earth*, 123, 7998–8015,  
1080 <https://doi.org/10.1029/2018JB016192>.
- 1081 Sato, K., Yamaji, A., 2006. Embedding stress difference in parameter space for stress tensor  
1082 inversion. *Journal of Structural Geology* 28, 957–971.  
1083 <https://doi.org/https://doi.org/10.1016/j.jsg.2006.03.004>
- 1084 Schulz, S.E. & Evans, J.P. 2000. Mesoscopic structure of the Punchbowl Fault, Southern  
1085 California and the geologic and geophysical structure of active strike-slip faults. *Journal*  
1086 *of Structural Geology*, 22, 913–930, [https://doi.org/https://doi.org/10.1016/S0191-  
1087 8141\(00\)00019-5](https://doi.org/https://doi.org/10.1016/S0191-8141(00)00019-5).
- 1088 Shan, Y., Fry, N., 2005. A hierarchical cluster approach for forward separation of heterogeneous  
1089 fault/slip data into subsets. *Journal of Structural Geology* 27, 929–936.  
1090 <https://doi.org/https://doi.org/10.1016/j.jsg.2005.02.001>

- 1091 Sherlock, S.C., Jones, K.A. & Park, R.G. 2008. Grenville-age pseudotachylite in the Lewisian:  
1092 laserprobe  $^{40}\text{Ar}/^{39}\text{Ar}$  ages from the Gairloch region of Scotland (UK). *Journal of the*  
1093 *Geological Society*, 165, 73–83, <https://doi.org/10.1144/0016-76492006-134>.
- 1094 Sherlock, S.C., Strachan, R.A., Jones, K.A., 2009. High spatial resolution  $^{40}\text{Ar}/^{39}\text{Ar}$  dating of  
1095 pseudotachylites: geochronological evidence for multiple phases of faulting within basement  
1096 gneisses of the Outer Hebrides (UK). *Journal of the Geological Society* 166, 1049–1059.  
1097 <https://doi.org/10.1144/0016-76492008-125>
- 1098 Sibson, R.H., 1980. Transient discontinuities in ductile shear zones. *Journal of Structural Geology* 2,  
1099 165–171. [https://doi.org/10.1016/0191-8141\(80\)90047-4](https://doi.org/10.1016/0191-8141(80)90047-4)
- 1100 Sibson, R.H., 1977a. Fault rocks and fault mechanisms. *Journal of the Geological Society* 133, 191–  
1101 213. <https://doi.org/10.1144/gsjgs.133.3.0191>
- 1102 Sibson, R.H., 1977b. The Outer Hebrides Thrust: Its structure, mechanism and deformation  
1103 environment. University of London.
- 1104 Sibson, R.H., 1975. Generation of pseudotachylite by ancient seismic faulting. *Geophysical Journal*  
1105 *of the Royal Astronomical Society* 43, 775. [https://doi.org/10.1111/j.1365-](https://doi.org/10.1111/j.1365-246X.1975.tb06195.x)  
1106 [246X.1975.tb06195.x](https://doi.org/10.1111/j.1365-246X.1975.tb06195.x)
- 1107 Simms, M.J. 2020. Discussion on ‘The Mesoproterozoic Stac Fada proximal ejecta blanket, NW  
1108 Scotland: constraints on crater location from field observations, anisotropy of magnetic  
1109 susceptibility, petrography and geochemistry’, &em&gt;*Journal of the Geological Society,*  
1110 *London&lt;/em&gt;*, 176, 830–846. *Journal of the Geological Society*, 177, 449 LP – 451,  
1111 <https://doi.org/10.1144/jgs2019-155>.
- 1112 Simms, M.J. & Ernstson, K. 2019. A reassessment of the proposed ‘Lairg Impact Structure’ and its  
1113 potential implications for the deep structure of northern Scotland. *Journal of the Geological*  
1114 *Society*, 176, 817 LP – 829, <https://doi.org/10.1144/jgs2017-161>.
- 1115 Simón, J.L., 2018. Forty years of paleostress analysis: has it attained maturity? *Journal of Structural*  
1116 *Geology*. <https://doi.org/https://doi.org/10.1016/j.jsg.2018.02.011>
- 1117 Smythe, D.K., Dobinson, A., McQuillin, R., Brewer, J.A., Matthews, D.H., Blundell, D.J., Kelk, B., 1982.  
1118 Deep structure of the Scottish Caledonides revealed by the MOIST reflection profile. *Nature*  
1119 299, 338–340.
- 1120 Spray, J.G., 1998. Localized shock- and friction-induced melting in response to hypervelocity impact.  
1121 In *Meteorites: Flux with Time and Impact Effects*, ed. MM Grady, R Hutchinson, GJH McCall, DA  
1122 Rothery, pp. 171–80. *Geol. Soc. London Spec. Pub.* 140:171–80
- 1123 Spray, J.G., 2010. Frictional Melting Processes in Planetary Materials: From Hypervelocity Impact to  
1124 Earthquakes. In: Jeanloz, R., Freeman, K.H. (Eds.), *Annual Review of Earth and Planetary*  
1125 *Sciences* 38, 221–254. <https://doi.org/10.1146/annurev.earth.031208.100045>
- 1126 Streule, M.J., Strachan, R.A., Searle, M.P., Law, R.D., 2010. Comparing Tibet-Himalayan and  
1127 Caledonian crustal architecture, evolution and mountain building processes. *Geological Society,*  
1128 *London, Special Publications* 335, 207–232. <https://doi.org/10.1144/sp335.10>

- 1129 Szulc, A.G., Alsop, G.I., Oliver, G.J.H., 2008. Kinematic and thermal constraints on the reactivation of  
1130 the Outer Hebrides Fault Zone, NW Scotland. *Geological Magazine* 145, 623–636.  
1131 <https://doi.org/10.1017/S0016756808004925>
- 1132 Thompson, L.M. & Spray, J.G. 1992. Pseudotachylytic rock distribution and genesis within the  
1133 Sudbury impact structure. *Geological Society of America Special Papers* , 293, 275–288,  
1134 <https://doi.org/10.1130/SPE293-p275>.
- 1135 Tien, Y.M., Kuo, M.C. & Juang, C.H. 2006. An experimental investigation of the failure mechanism of  
1136 simulated transversely isotropic rocks. *International Journal of Rock Mechanics and Mining*  
1137 *Sciences*, 43, 1163–1181, <https://doi.org/https://doi.org/10.1016/j.ijrmms.2006.03.011>.
- 1138 Wallace, R.E., 1951. Geometry of Shearing Stress and Relation to Faulting. *The Journal of Geology* 59,  
1139 118–130. <https://doi.org/10.1086/625831>
- 1140 Wallis, D., Lloyd, G.E., Phillips, R.J., Parsons, A.J., Walshaw, R.D., 2015. Low effective fault strength  
1141 due to frictional-viscous flow in phyllonites, Karakoram Fault Zone, NW India. *Journal of*  
1142 *Structural Geology* 77, 45–61. <https://doi.org/http://dx.doi.org/10.1016/j.jsg.2015.05.010>
- 1143 Wallis, D., Phillips, R.J., Lloyd, G.E., 2013. Fault weakening across the frictional-viscous transition  
1144 zone, Karakoram Fault Zone, NW Himalaya. *Tectonics* 32, 1227–1246.  
1145 <https://doi.org/10.1002/tect.20076>
- 1146 Walsh, J.J., Childs, C., Imber, J., Manzocchi, T., Watterson, J., Nell, P.A.R., 2003. Strain localisation  
1147 and population changes during fault system growth within the Inner Moray Firth, Northern  
1148 North Sea. *Journal of Structural Geology* 25, 307–315.  
1149 [https://doi.org/http://dx.doi.org/10.1016/S0191-8141\(02\)00028-7](https://doi.org/http://dx.doi.org/10.1016/S0191-8141(02)00028-7)
- 1150 White, J.C., 1996. Transient discontinuities revisited: pseudotachylyte, plastic instability and the  
1151 influence of low pore fluid pressure on deformation processes in the mid-crust. *Journal of*  
1152 *Structural Geology* 18, 1471–1486. [https://doi.org/10.1016/s0191-8141\(96\)00059-4](https://doi.org/10.1016/s0191-8141(96)00059-4)
- 1153 White, S.H., Glasser, J., 1987. The Outer Hebrides Fault Zone: evidence for normal movements.  
1154 *Geological Society, London, Special Publications* 27, 175–183.  
1155 <https://doi.org/10.1144/gsl.sp.1987.027.01.15>
- 1156 Whitehouse, M.J. & Bridgwater, D. 2001. Geochronological constraints on Paleoproterozoic crustal  
1157 evolution and regional correlations of the northern Outer Hebridean Lewisian complex,  
1158 Scotland. *Precambrian Research*, 105, 227–245,  
1159 [https://doi.org/http://dx.doi.org/10.1016/S0301-9268\(00\)00113-3](https://doi.org/http://dx.doi.org/10.1016/S0301-9268(00)00113-3).
- 1160 Xu, S.-S., Nieto-Samaniego, A.F. and Alaniz-Álvarez, S.A. 2009. Quantification of true displacement  
1161 using apparent displacement along an arbitrary line on a fault plane. *Tectonophysics* 467, 107–118.
- 1162 Yamada, E. & Sakaguchi, K. 1995. Fault-slip calculation from separations. *Journal of*  
1163 *Structural Geology*, 17, 1065–1070, [https://doi.org/https://doi.org/10.1016/0191-](https://doi.org/https://doi.org/10.1016/0191-8141(95)00003-V)  
1164 [8141\(95\)00003-V](https://doi.org/https://doi.org/10.1016/0191-8141(95)00003-V).
- 1165 Žalohar, J., Vrabec, M., 2007. Paleostress analysis of heterogeneous fault-slip data: The Gauss

1166 method. *Journal of Structural Geology* 29, 1798–1810.  
1167 <https://doi.org/https://doi.org/10.1016/j.jsg.2007.06.009>  
1168

<b>Deformation phase</b>	<b>Kinematics</b>	<b>Deformation style and fault rock types</b>	<b>Location(s) observed</b>	<b>Reference</b>
Pre-Caledonian (Late Laxfordian, 1.7 Ga, or Grenvillian, 1.1 Ga)	Top-to-NW thrusting	Ductile shear	Lewis & Harris	Butler et al. (1995) Imber et al. (2001)
	Top-to-E extension (?)	Observed only as offshore growth strata in Torridon Group	Much of OHFZ	Imber et al. (2001)
Caledonian compression	Top-to NW thrusting	Ductile shear	Lewis & Harris	Sibson (1977)
			South Uist	Osinski et al. (2001)
			Barra	MacInnes et al. (2000)
	Top-to NNW/NW/WNW (E-W compression?)	Brittle thrust faulting (cataclasites and pseudotachylytes)	Much of OHFZ	Imber et al. (2001) Butler et al. (1998) Sibson (1977)
			South Uist	Osinski et al. (2001)
			Barra	MacInnes et al. (2000)
(Late) Caledonian strike-slip	Top-to-NE sinistral (oblique)	Phyllonite shear zones	Scalpay	Szulc et al. (2008)
			Much of OHFZ	Imber et al. (2001) Butler et al. (1998)
	Dextral and sinistral (limited observations)	Small displacement slip surfaces along phyllonite foliation	South Uist	Osinski et al. (2001)
	Dextral and sinistral	Brittle faulting (with pseudotachylytes)	Barra	MacInnes et al. (2000)
Late Caledonian extension	Top-to-S, -E or SE extensional	Shear of phyllonites and brittle slip along phyllonite foliation	Much of OHFZ	Imber et al. (2001)
	Top-to-ENE, -NE and top-to-ESE extensional	Shear of phyllonites, brittle faults (with pseudotachylytes), localised detachment faults	South Uist	Osinski et al. (2001)
	Top-to-ESE and	Shear of phyllonites, steep brittle faults	Barra	MacInnes et al.

	-E extensional	(with pseudotachylytes) and shallow detachments		(2000)
--	----------------	---	--	--------

1170 Table. 1: Existing structural framework for deformation along the OHFZ

1171

1172 Figure 1. Geological map of the Outer Hebrides (Western Isles), UK, showing key lithological units  
1173 (after Fettes et al., 1981) and location of faults relevant to discussion (selected from Sibson, 1977b;  
1174 Fettes et al., 1981, 1992; Brewer and Smythe, 1986). Indication of pseudotachylyte localities shown  
1175 by black circles (selected from Fettes et al., 1992; MacInnes et al., 2000, plus those observed in  
1176 current study). Stereonets (lower hemisphere, equal area) show poles-to-planes of pseudotachylyte  
1177 generation planes; top left plot covers the whole OHFZ region whilst additional plots are subset by  
1178 local region. Kamb contours show density increments as indicated in the respective legend. The  
1179 regional dip of the OHFZ is indicated on each plot via a black great-circle and black pole whilst the  
1180 local trend for each region is indicated by grey ticks.

1181 Figure 2. Typical features of OHFZ pseudotachylytes. (a) Pseudotachylyte fault vein (generation  
1182 plane) and injections into host rock, North Uist [BNG 86113 86662]; (b) Fault breccia with  
1183 pseudotachylyte matrix, South Uist [BNG 75692 823056]; (c) Back-scattered electron image of  
1184 pseudotachylyte vein displaying radiating plagioclase microlites around unmelted clasts of quartz  
1185 and plagioclase, within ultrafine matrix of plagioclase, hornblende, biotite and iron oxide; (d) back-  
1186 scattered electron image of pseudotachylyte ('PST') vein margin with strong spherulitic texture.

1187

1188 Figure 3. Field and microstructural evidence for slip sense on pseudotachylyte faults. (a)  
1189 pseudotachylyte fault displaying apparent normal, top-down-to-south east displacement of  
1190 shallower-dipping pseudotachylyte vein [BNG 130028 917107]; (b) Overlay over (a) illustrating the  
1191 two phases of pseudotachylyte; (c) pseudotachylyte faults with apparent reverse top-to-NE and top-  
1192 to-SW offset of amphibolite layers [BNG 85626 856188]; (d) Overlay over (c) showing thin  
1193 pseudotachylyte faults offsetting amphibolite banding; (e) Backscattered electron image of  
1194 pseudotachylyte ('PST') vein with shape preferred orientation of quartz (darker grey) and plagioclase  
1195 clasts suggesting top-to-left (east) apparent slip; (f) Cataclastic margin within vein with S-C type  
1196 foliation picked out by pseudotachylyte ingress indicating top-to-left slip (top-to-SW).

1197

1198 Figure 4. Dynamic off-fault tensile crack model for pseudotachylyte injection veins. (a) Sequence of  
1199 near-parallel injection veins (arrowed) restricted to single wall of pseudotachylyte fault [BNG 30388  
1200 16447]; (b) Overlay over (a) showing pseudotachylyte fault and injection vein geometry; (c)  
1201 Sequence of inclined near-parallel injection veins restricted to single wall of pseudotachylyte fault  
1202 [BNG 65624 803536]; (d) Overlay over (c) showing pseudotachylyte fault and injection vein  
1203 geometry; (e) Model of dynamic tensile injections showing how local rupture tip stress fields can  
1204 induce coseismic tensile cracking (after Dalguer et al., 2003); (f) Determination of slip plunge and  
1205 azimuth (white arrow) from the resolved normal to the injection vein dip, and slip sense from  
1206 identifying the acute angle between injection veins and the fault plane.

1207

1208 Figure 5. En-echelon injection vein systems. (a) cross-cutting arrays of pseudotachylyte injection  
1209 veins [horizontal section, BNG 66008 803981]; (b) Diffuse array of en-echelon veins [horizontal  
1210 section, BNG 65687 803437]; (c) Linear array of en-echelon veins [horizontal section, BNG 70537  
1211 799802]; (d) Example of pseudotachylyte fault vein with injection vein segmenting at injection tip  
1212 [vertical section, BNG 79497 810173]; (e) Pebble rotated 180° to show segmentation of single  
1213 injection vein into en-echelon system.

1214 Figure 6. Model of en-echelon pseudotachylyte injection vein formation. (a) Planar tensile fracture  
1215 (or injection vein) propagating with no deviation in stress field; (b) En-echelon segmentation of  
1216 fracture (or injection vein) in response to shear experienced at the propagating tip. Such mixed  
1217 mode behaviour can form a response to a spatial and/or temporal change in stress field orientation  
1218 (after Clemente et al., 2007); (c) Application of the en-echelon model to a dynamic tensile  
1219 pseudotachylyte injection vein propagating away from the fault plane. Initially the vein is oriented  
1220 relative to the slip direction and the dynamic rupture tip stress field, but this influence falls away as  
1221 the rupture tip moves on and the injection vein propagates away from the fault.

1222 Figure 7. Apparent slip sense and fault dip observed from offset markers across pseudotachylyte  
1223 fault veins in the field (n = 29) and microstructural indicators from fault veins observed in thin  
1224 section, where the vein orientation was known (n = 7).

1225 Figure 8. Large stereonet (right hand side) show the stress fields resulting from palaeostress  
1226 analysis and the faults that are mechanically attributable to them. Hangingwall slip directions are  
1227 indicated with arrows. The relative stress state for the faults attributable to each stress field is  
1228 shown plotted on a dimensionless Mohr's circle to confirm the mechanical compatibility. The fault  
1229 plane solutions for individual faults in the dataset are plotted with the fault plane in bold black.  
1230 These slip solutions (focal mechanisms) are block-coloured to correspond to the stress field with  
1231 which they are attributable to - grey shaded solutions were not compatible with any of the resulting  
1232 stress fields (\* indicates a slip solution which is mechanically attributable to both the orange and the  
1233 pink stress fields). Also shown is the fault plane solution resulting from AMS analysis (Ferré et al.,  
1234 2016). Turquoise shading on the map indicates presence of phyllonite belts (after Imber, 1998).

1235 Figure 9. Results from en-echelon array observations: (a) Orientation of perpendicular to en-echelon  
1236 arrays (array-normals); (b) orientation of perpendicular to en-echelon segments (segment-normals);  
1237 (c) magnitude and direction of segment rotation relative to the parent array/vein, by array  
1238 orientation.

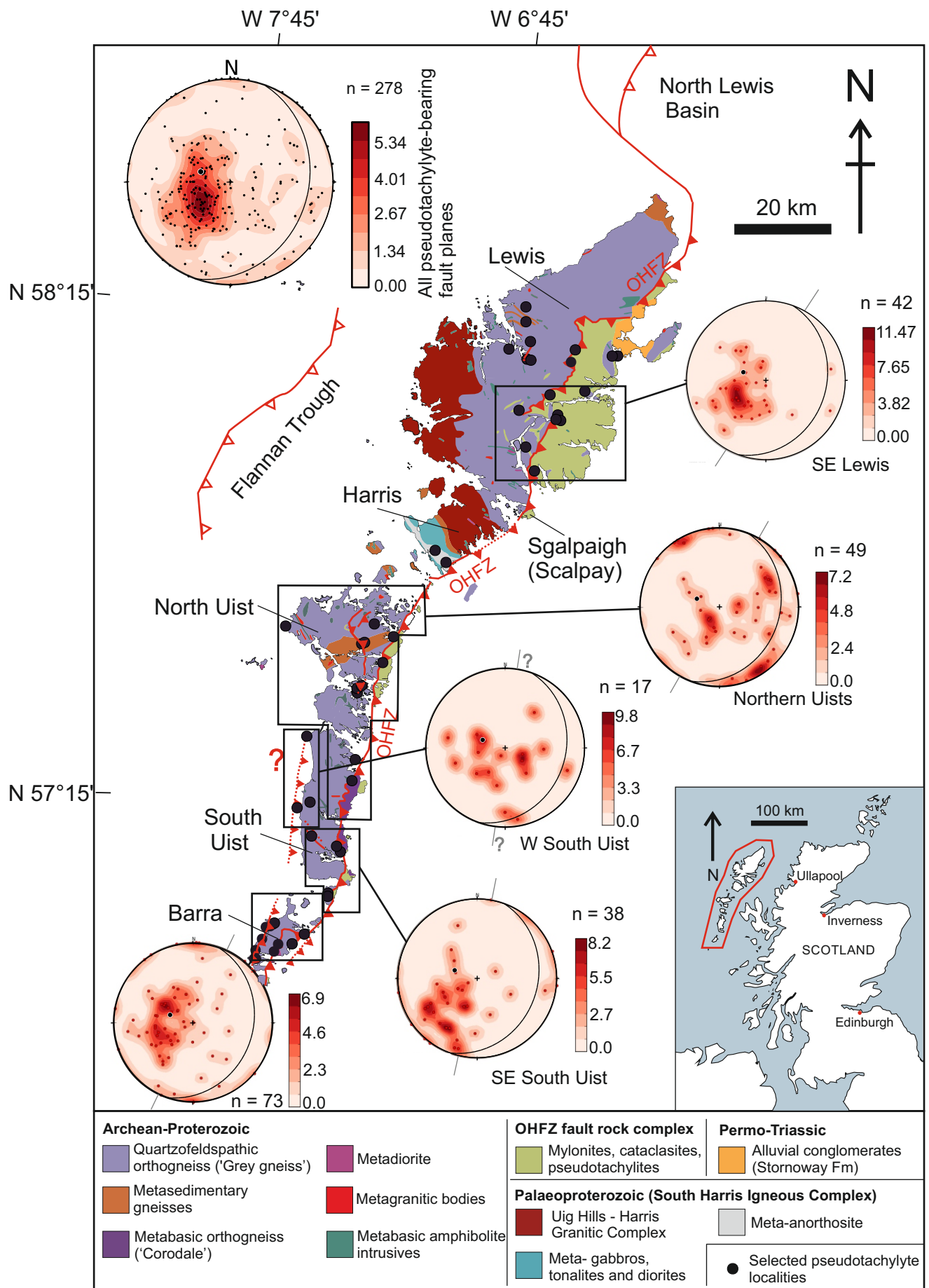
1239 Figure 10. Maps of localities where multiple en-echelon arrays are observed, indicating the segment-  
1240 normal (the propagation trajectory of which is rotating to be compliant with  $\sigma_3$ ) and the sense of  
1241 deviation (clockwise or anticlockwise) relative to the whole en-echelon array. Geological units after  
1242 Fettes et al. (1981); base maps from © OpenStreetMap contributors  
1243 (<https://www.openstreetmap.org/copyright>).

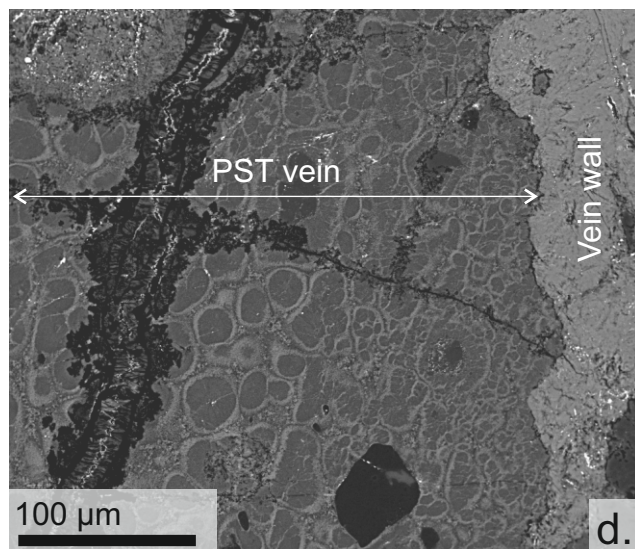
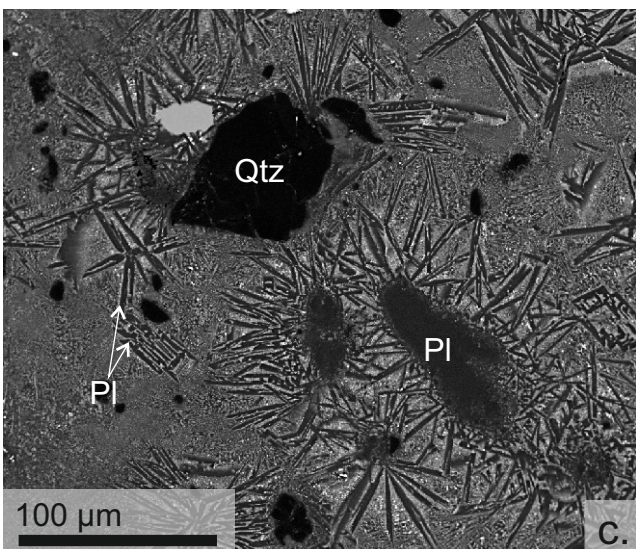
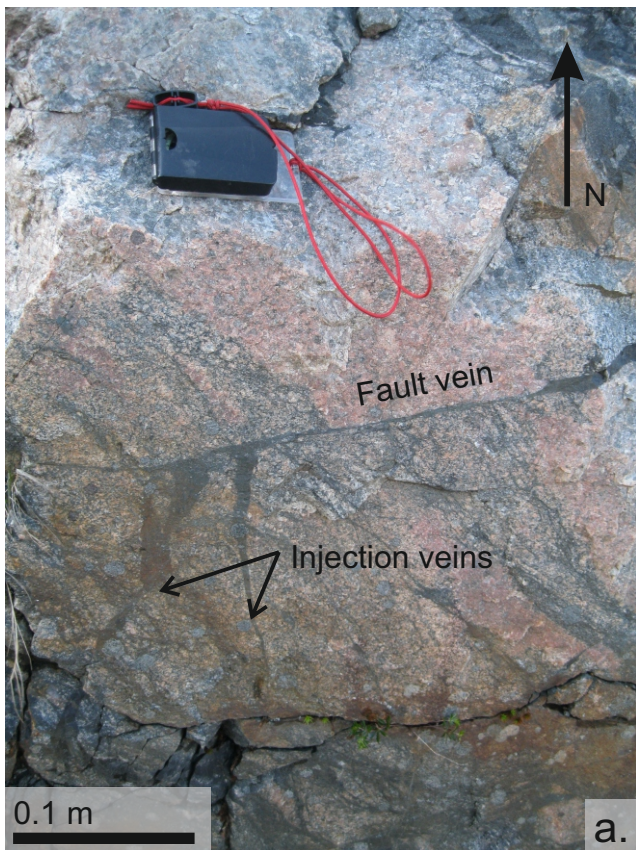
1244 Figure 11. Acute angle between pseudotachylyte-bearing fault and surrounding foliation (n = 67).

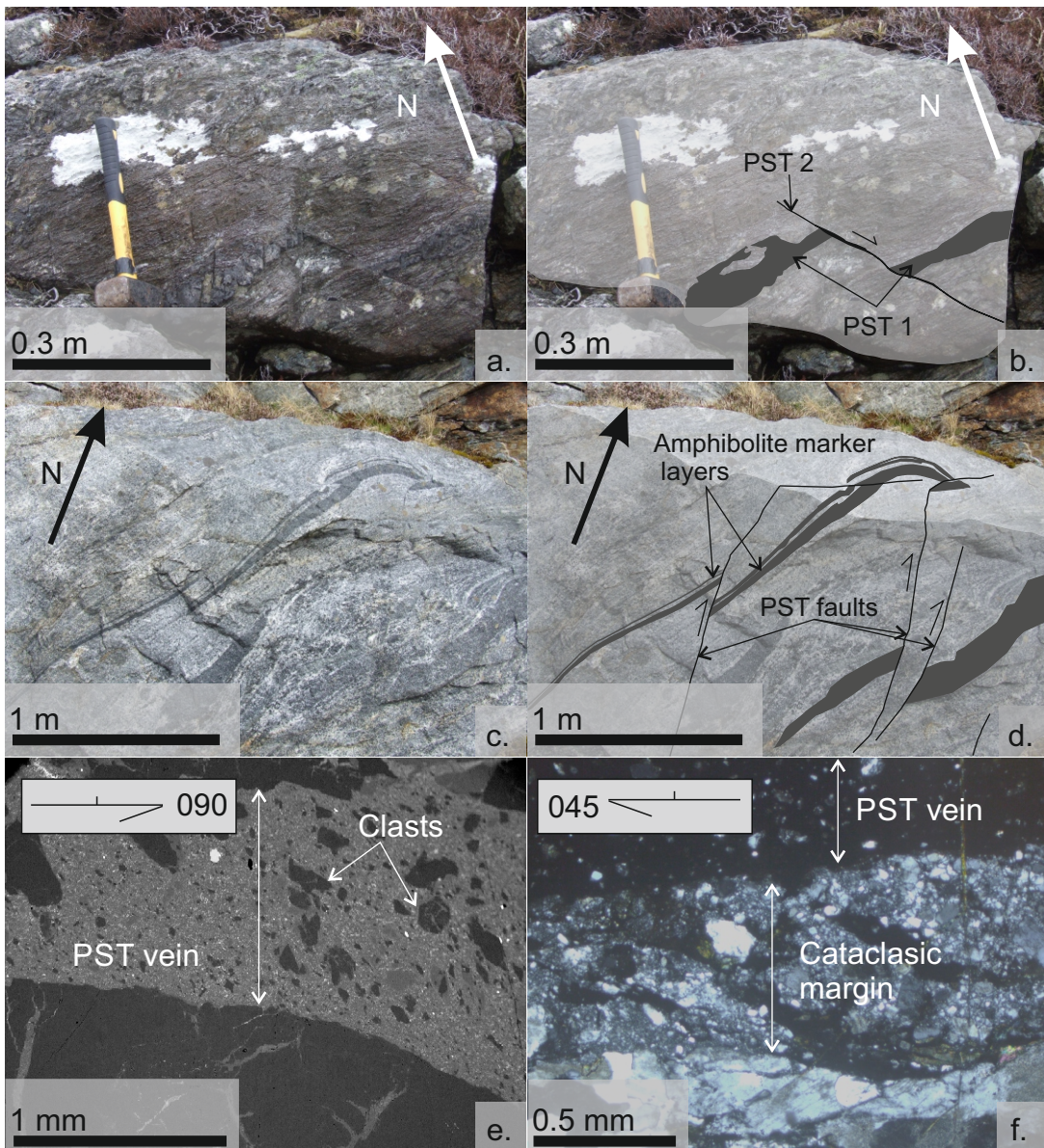
1245 Figure 12. Schematic illustration of deformation events which may have contributed to the record of  
1246 seismic ruptures around the Outer Hebrides, resulting in the record of scattered and variously  
1247 oriented pseudotachylyte – bearing faults. Suggested stress fields are sourced from palaeostress  
1248 analysis (Fig. 8). Dates for meteorite impact are taken from Reddy et al. (2015) and for early  
1249 mainland faulting from Sherlock et al. (2009) and Holdsworth et al. (2020).

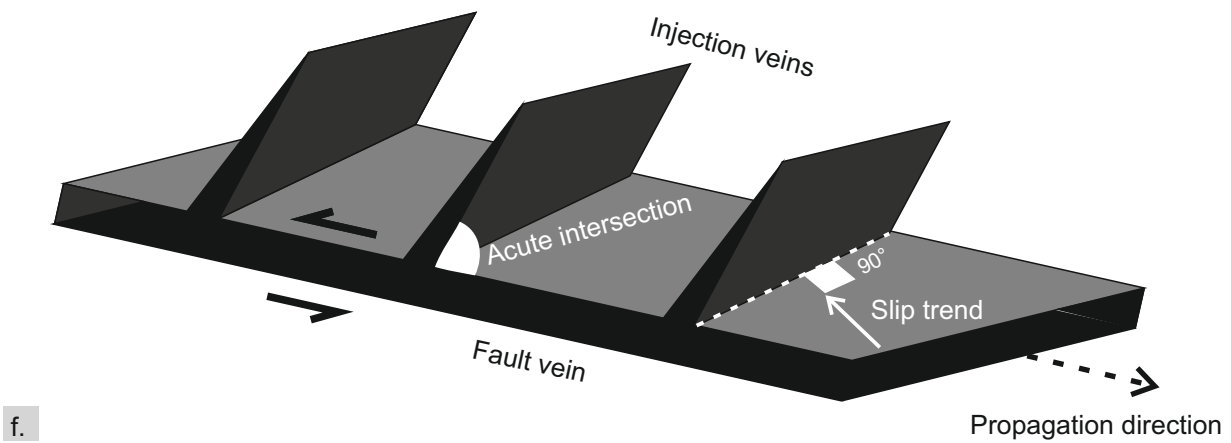
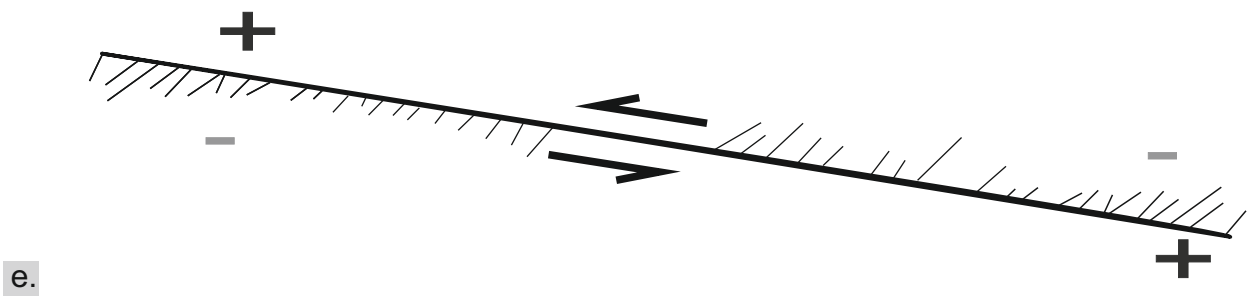
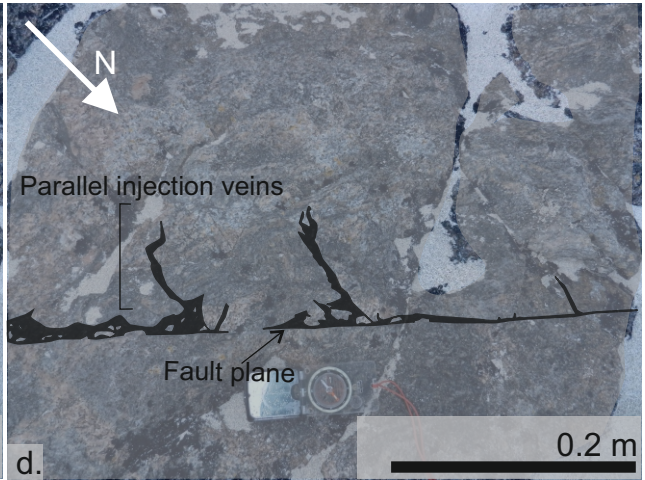
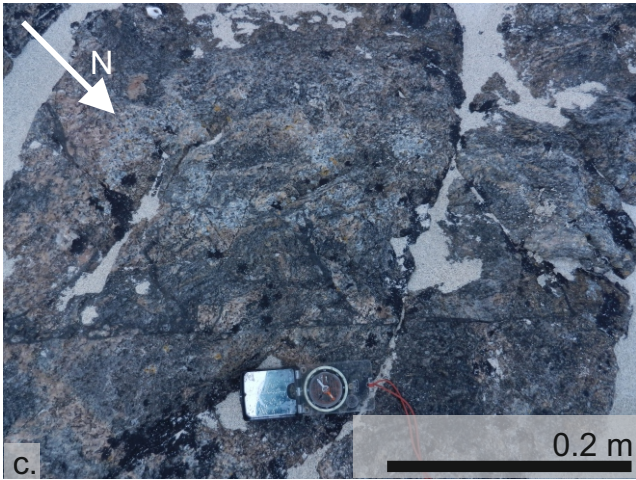
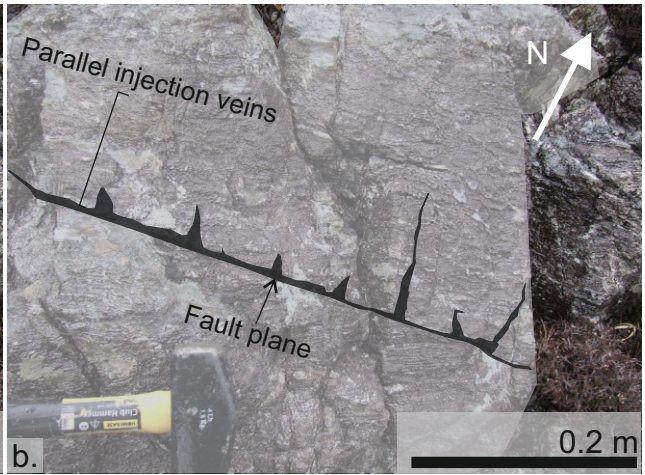
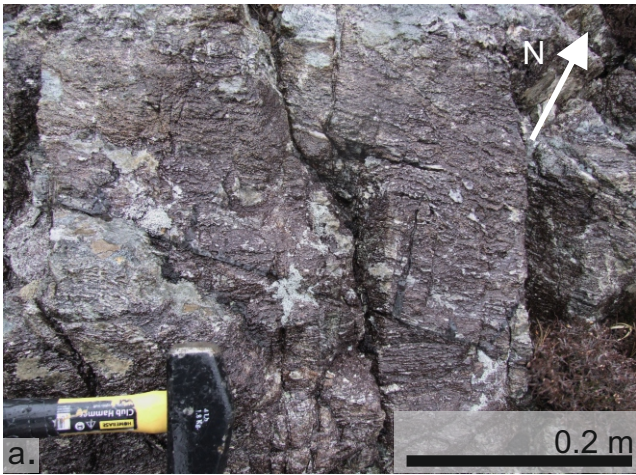
1250

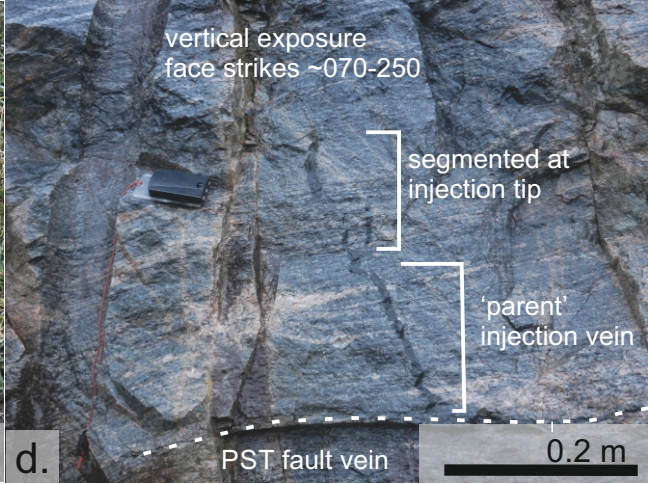
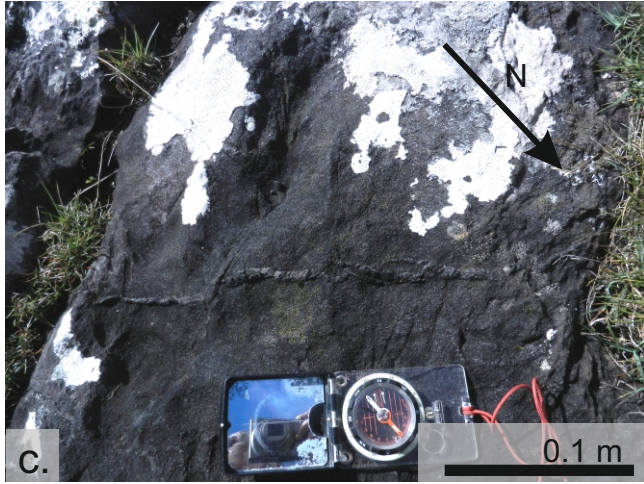
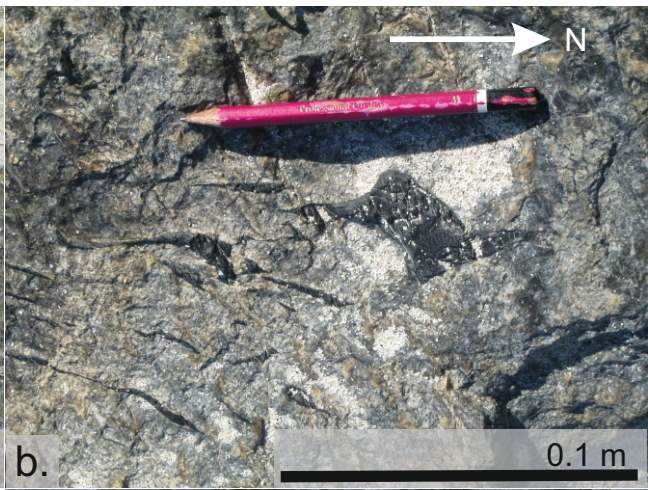
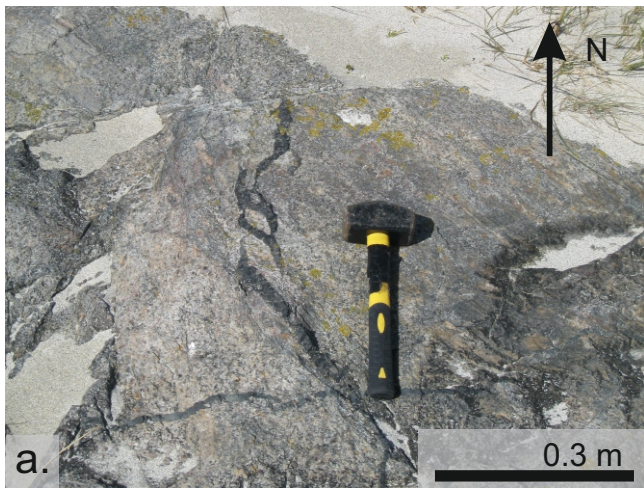




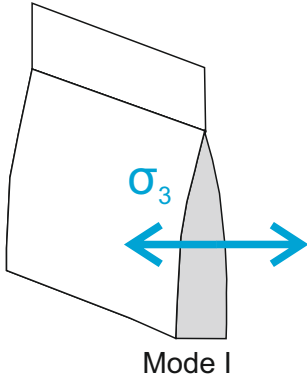




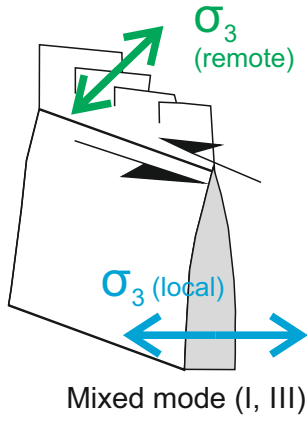




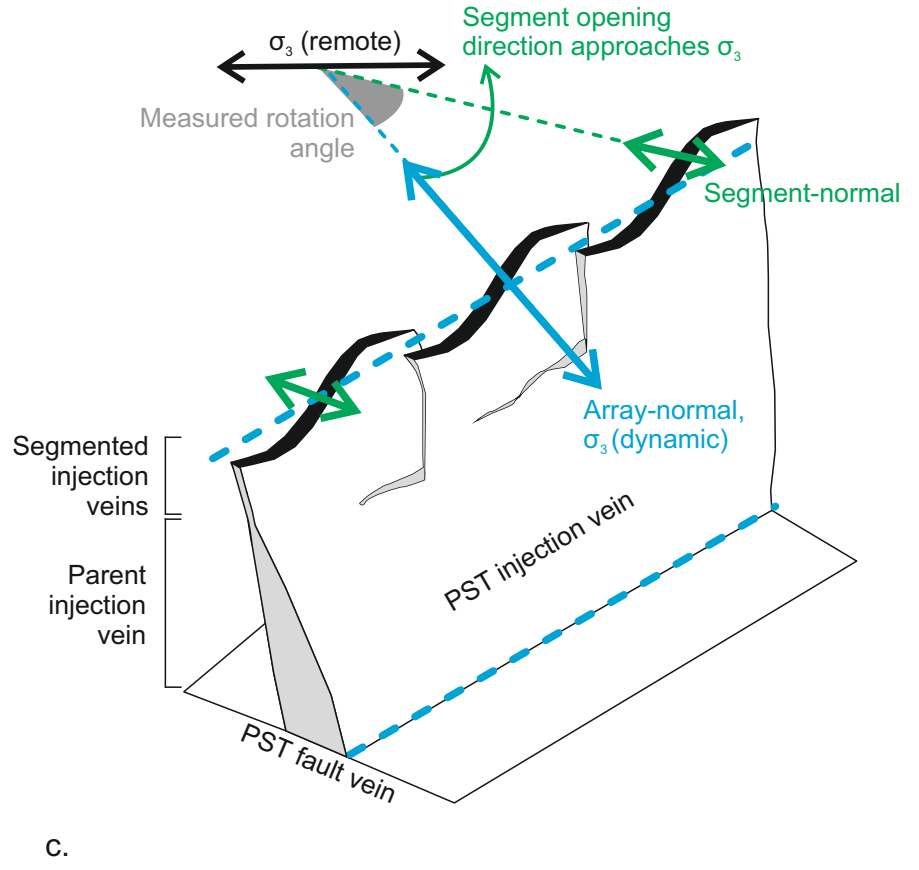
### Planar fracture

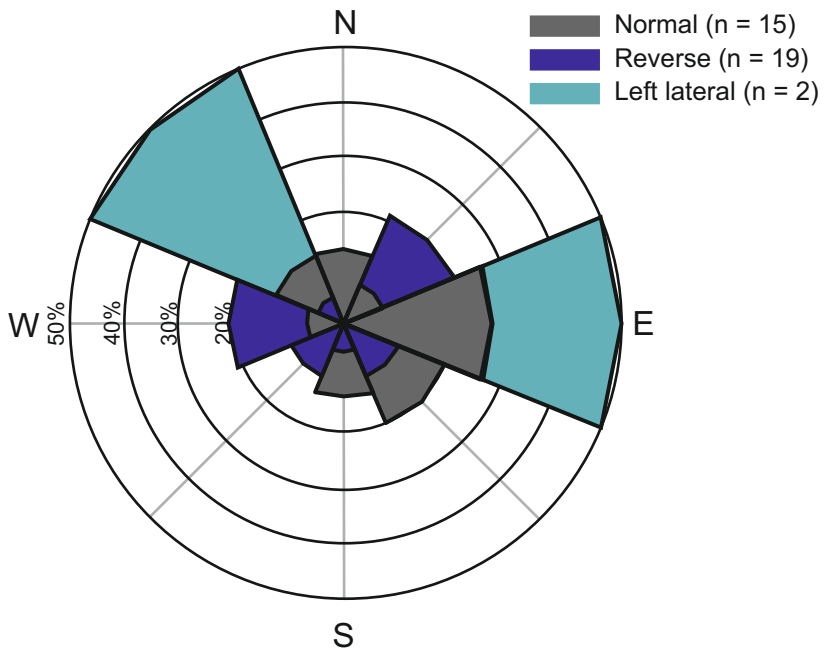


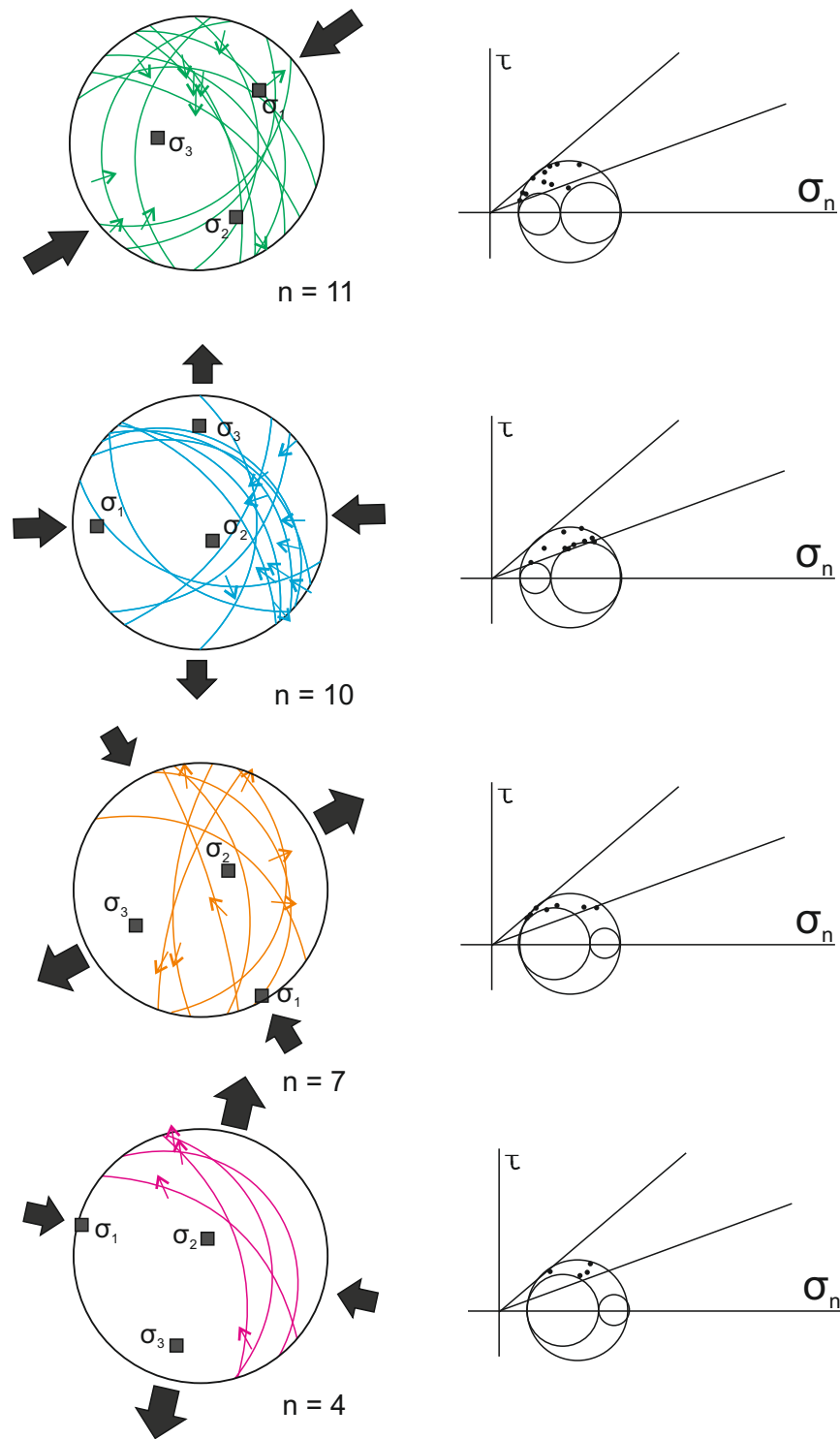
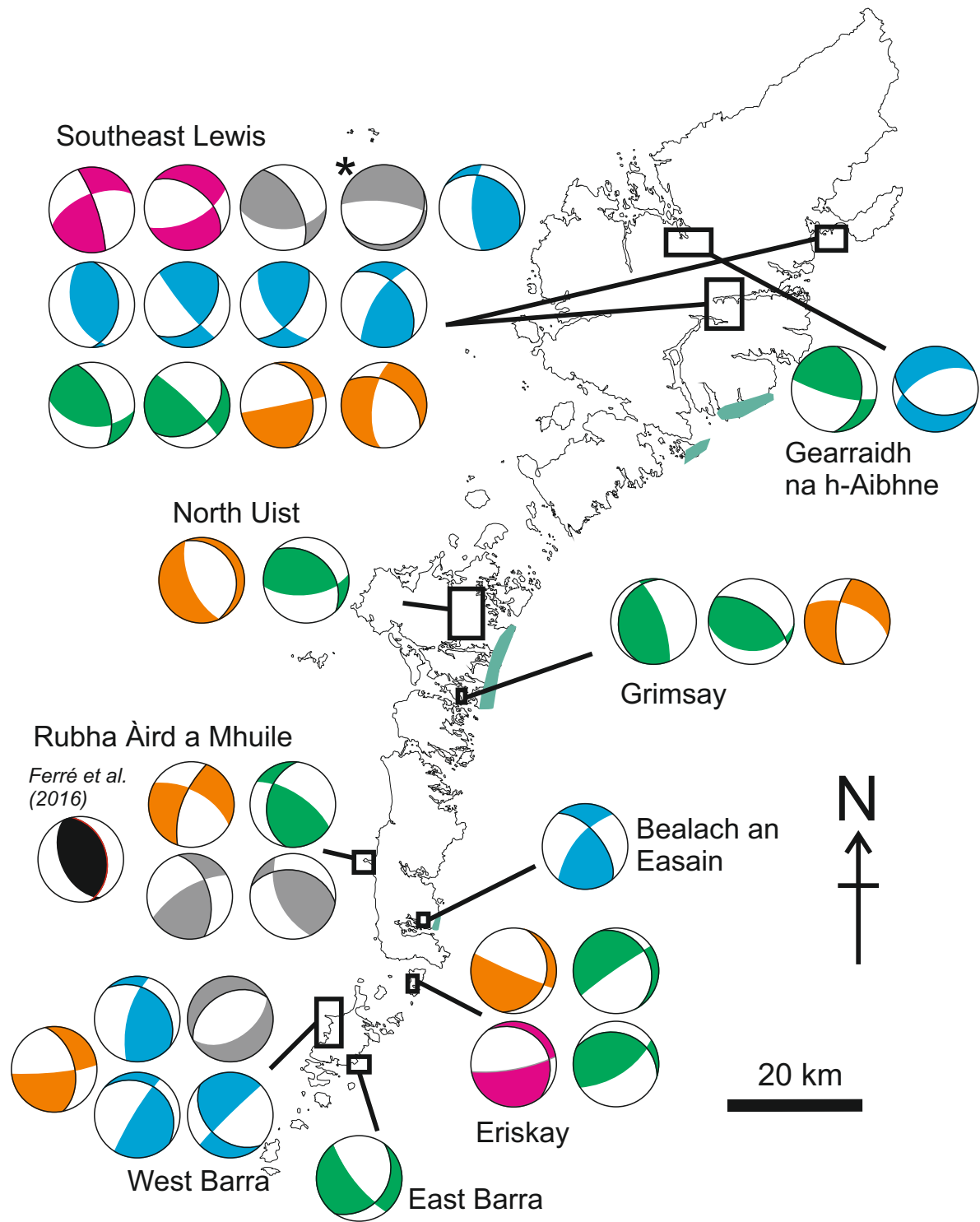
### En-echelon segments



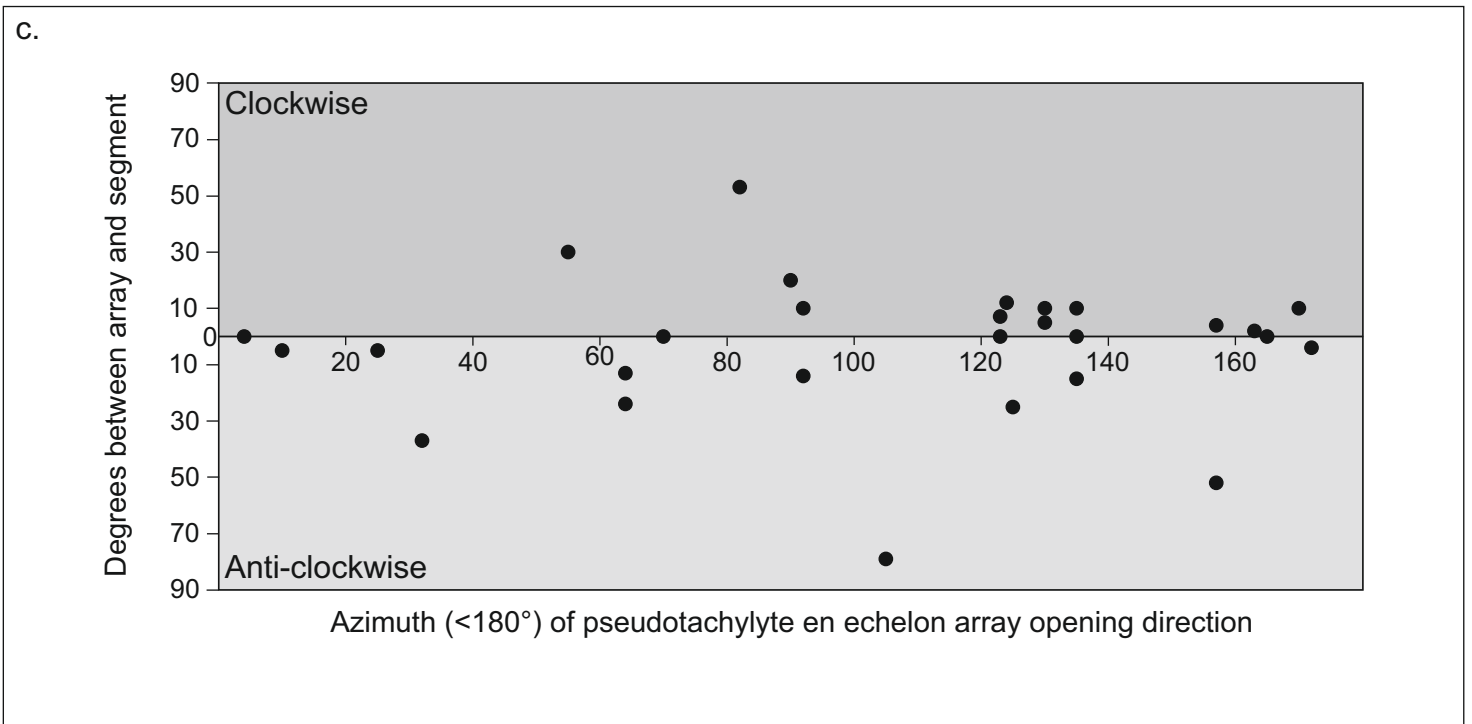
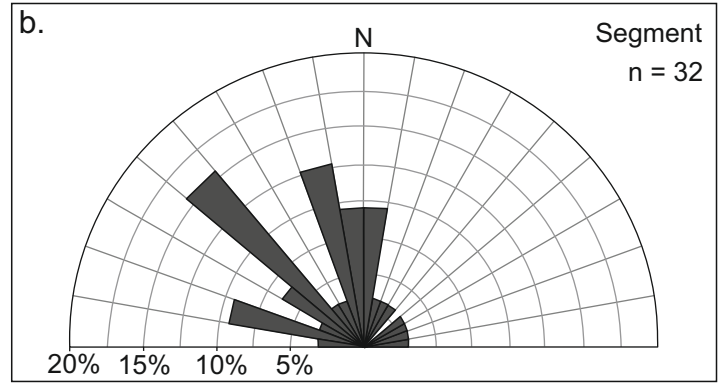
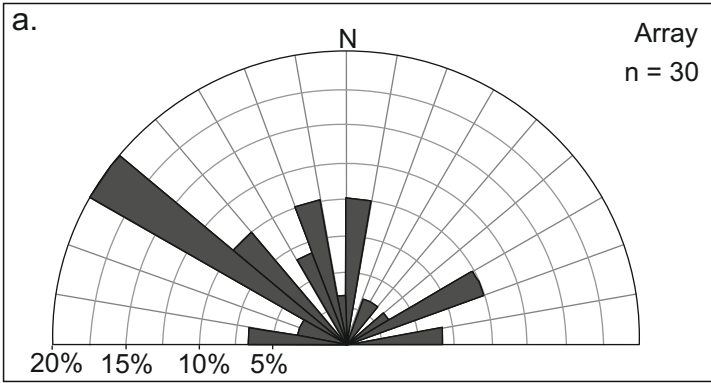
### En echelon pseudotachylyte injection veins









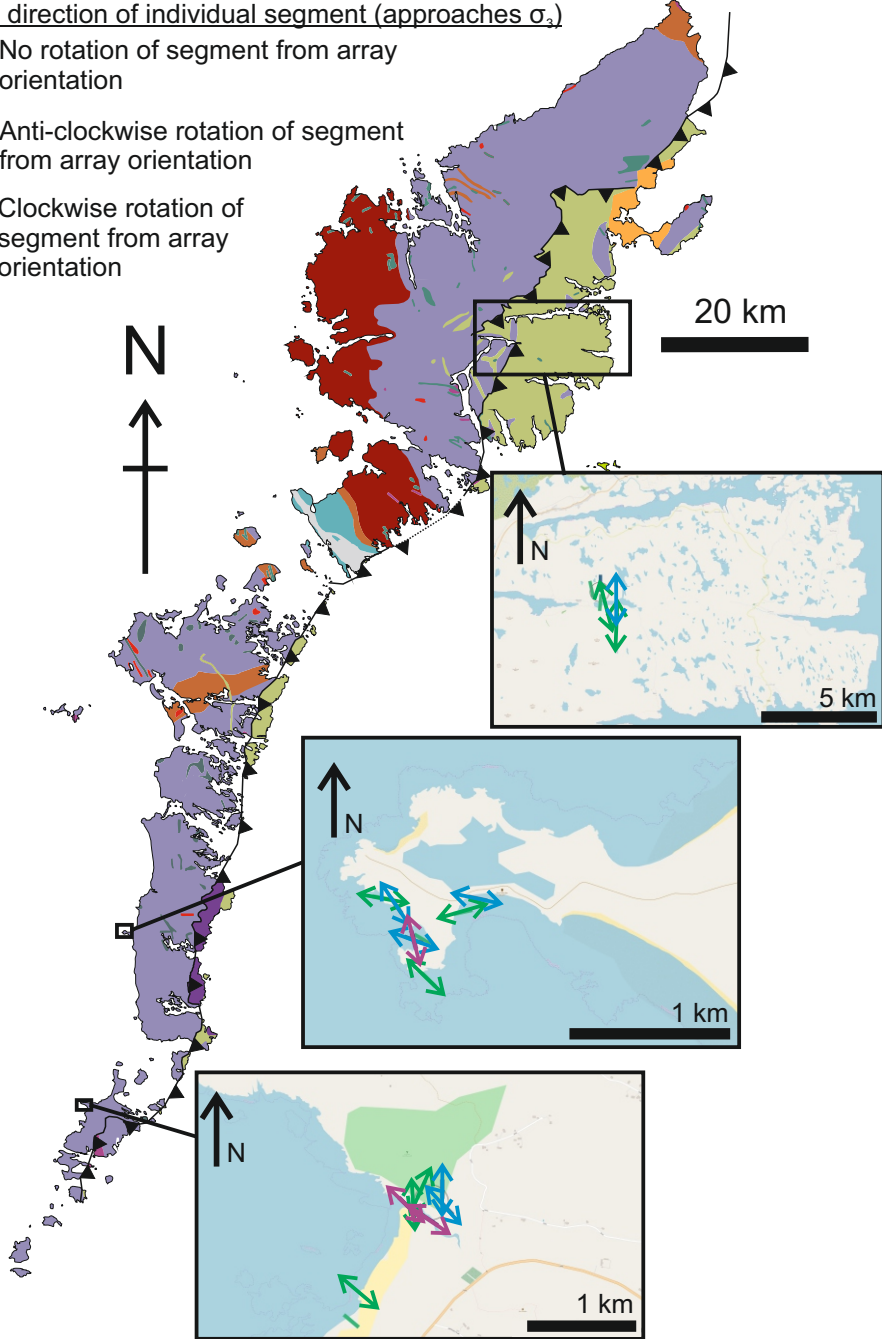


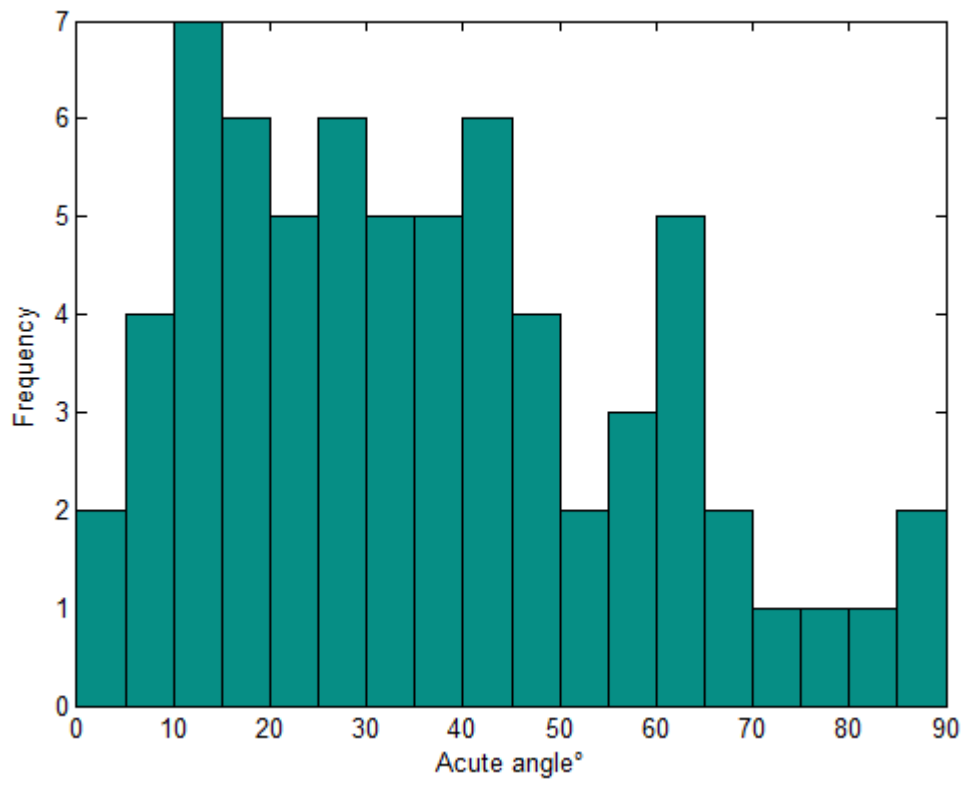
Opening direction of individual segment (approaches  $\sigma_3$ )

↔ No rotation of segment from array orientation

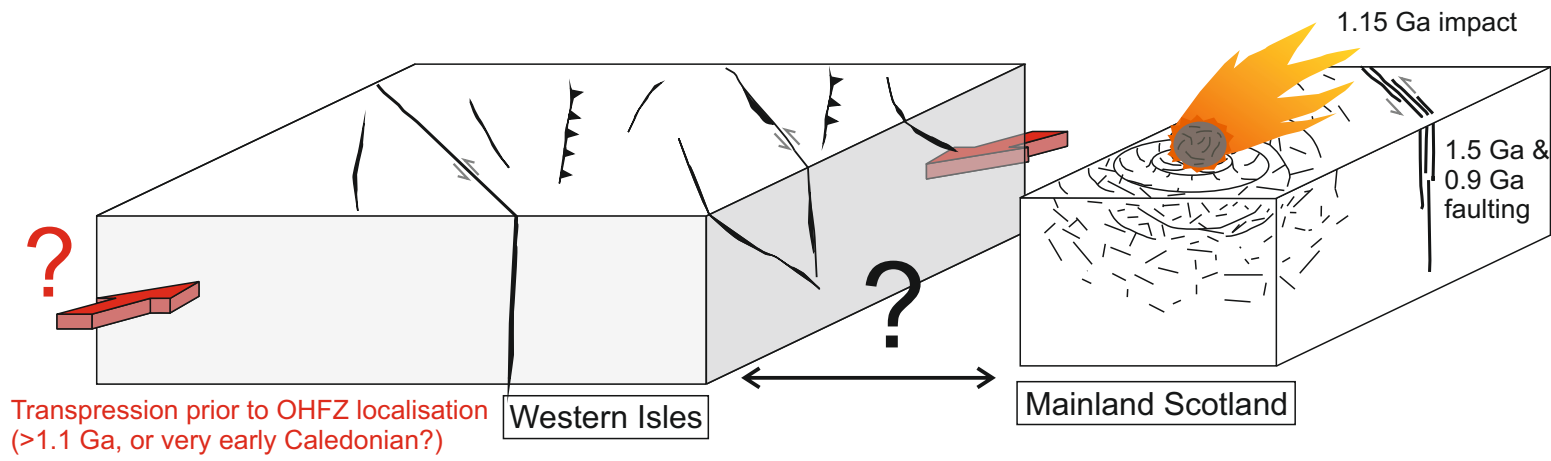
↺ Anti-clockwise rotation of segment from array orientation

↻ Clockwise rotation of segment from array orientation





1. Possible pre-OHFZ events



2. OHFZ faulting under variable stress fields

